CME LIVE OPEN ACCESS

Journal of
Applied Mechanics Reviews and Reports

Research Article ISSN: 3069-0803

The Digital Twin of a Quenched Gear: Predicting Residual Stress and Hardness Through Multiphysics Simulation

Mohammad Yaghoub Abdollahzadeh Jamalabadi*

Department of Marine Engineering, Chabahar Maritime University, Chabahar, Iran.

Corresponding Author: Mohammad Yaghoub Abdollahzadeh Jamalabadi, Department of Marine Engineering, Chabahar Maritime University, Chabahar, Iran.

Received: 2026 Apr 01 **Accepted:** 2026 Apr 20 **Published:** 2026 May 05

Abstract

This paper presents a systematic parameter study of carburization and quenching for a 2D steel spur gear (pitch diameter 100 mm, 20 teeth) using coupled multiphysics finite element simulation. The investigation examines four key process parameters—carbon potential (0.55–0.95 wt.%), mass transfer coefficient (0.5–5.0×10^{-5} cm/s), carburization duration (4–24 h), and quench oil heat transfer coefficient (1000–5000 W/m^2•K)—on carbon concentration profiles, martensite start temperature distributions, phase fractions, residual stress fields, and Effective Case Depth (ECD). A complete four-step computational chain derives ECD: (1) Fickian diffusion with Robin boundary conditions solved by finite differences; (2) carbon-dependent M_s mapping (M_s = 560 − 470c); (3) Koistinen-Marburger martensite fraction model; and (4) Maynier hardness formulation, yielding baseline ECD = 1.636 mm at the ISO 2639/AGMA 2101 threshold of 550 HV. The framework is validated against 20 peer-reviewed studies (2022–2025). Results demonstrate that carbon potential and carburization time exert dominant influence on case depth (sensitivity indices S_i = 1.6–1.8 and 1.2, respectively), while quench oil severity primarily governs residual stress magnitude at the tooth root (S_i = 1.6). The 115-second transformation time differential between core and surface M_s crossings quantifies the compressive stress mechanism. ECD sensitivity analysis confirms approximate $\sqrt{t}$ scaling with carburization time, establishing quantitative process design charts for the 100 mm gear geometry. The study concludes with synthesis of research gaps identified in current literature, including latent heat effects, tensor-valued transformation plasticity, and 3D geometry requirements.

Keywords: Carburization, Quenching, Steel Gear, Effective Case Depth, ECD, ISO 2639, AGMA 2101, Fick Diffusion, Koistinen Marburger, Maynier Hardness, TRIP, Residual Stress

1. Introduction

Case hardening by carburization followed by quenching is one of the most widely employed thermochemical surface treatments in the gear manufacturing industry. Gears are fundamental power-transmission elements in automotive drivetrains, wind turbines, aerospace gearboxes, and industrial machinery, whose reliable performance under cyclic bending at the tooth root and Hertzian contact at the tooth flank demands simultaneously high surface hardness, wear resistance, and tough core microstructure — a combination achievable only through carburization-quenching [1]. The process involves two physically distinct stages: (1) a high-temperature diffusion cycle in which carbon migrates from a carbon-rich atmosphere into the austenitic steel surface via Fick diffusion, establishing a carbon concentration gradient that determines subsequent phase transformation temperatures; and (2) rapid cooling in an oil or polymer quenchant that drives martensitic phase transformation.

The primary engineering design parameter arising from the carburization-quenching process is the Effective Case Depth (ECD) — the perpendicular distance from the gear tooth surface to the point where the Vickers hardness drops below 550 HV, as standardized in ISO 2639 and AGMA 2101. ECD quantifies the extent of the hardened layer and is the primary design parameter for both tooth root bending fatigue resistance and contact (pitting) fatigue resistance. However, ECD cannot be read directly from the simulation output: it must be derived through a four-step computational chain linking the carbon diffusion field to the martensite fraction via the Koistinen-Marburger model, and then to Vickers hardness via the Maynier empirical formula. This derivation chain and its seven diagnostic figures are developed in Section 4 of this paper. The fatigue performance of case-hardened gears is further governed by the residual stress field developed during quenching. Zhang et al demonstrated through detailed finite element analysis that the carbon-induced Ms gradient — not the thermal gradient alone — is responsible for the characteristic surface compressive stress state [2]. Sun et al quantified this benefit, showing that compressive residual stresses of approximately −280 to

−400 MPa at the tooth root can extend total bending fatigue life by a factor of 2–4 [3].

The recent contributions on induction hardening (Jamalabadi, gear heat treatment (Jamalabadi), and machine learning in tribology (Marian & Tremmel) whose employed numerical techniques inform the multiphysics framework [4-6]. The mathematical foundation of the carburization process is Fick's second law of diffusion: $\partial c/\partial t + \nabla\bullet(-D_c\nabla c) = 0$. Carbon transport from the gas phase is modeled by a Robin boundary condition: $n\bullet(-D_c\nabla c) = k_c(c_{env} - c)$. Salawu et al validated this formulation experimentally across multiple carburizing agents, demonstrating good agreement between Fick’s law predictions and measured carbon profiles in grey cast iron [7]. Hiremath et al showed that Cr and Mn alloying elements reduce effective Dc by up to 25% relative to plain carbon steel, justifying alloy-specific tabular diffusivity values [8]. Jamalabadi applied analogous coupled diffusion-phase-transformation modeling to induction hardening of cylindrical steel pins, validating the Robin boundary condition framework for convective quenching scenarios [4]. Kochmański et al showed that Ni additions (1.5–3.0 wt.%) increase retained austenite without changing case depth, highlighting that diffusion and transformation outcomes can decouple when alloy composition is varied [9]. Liu et al further extended the diffusion modeling framework by incorporating carburizing expansion strain and dynamic thermal boundary conditions to predict quenching deformation of gears with mandrels [10].

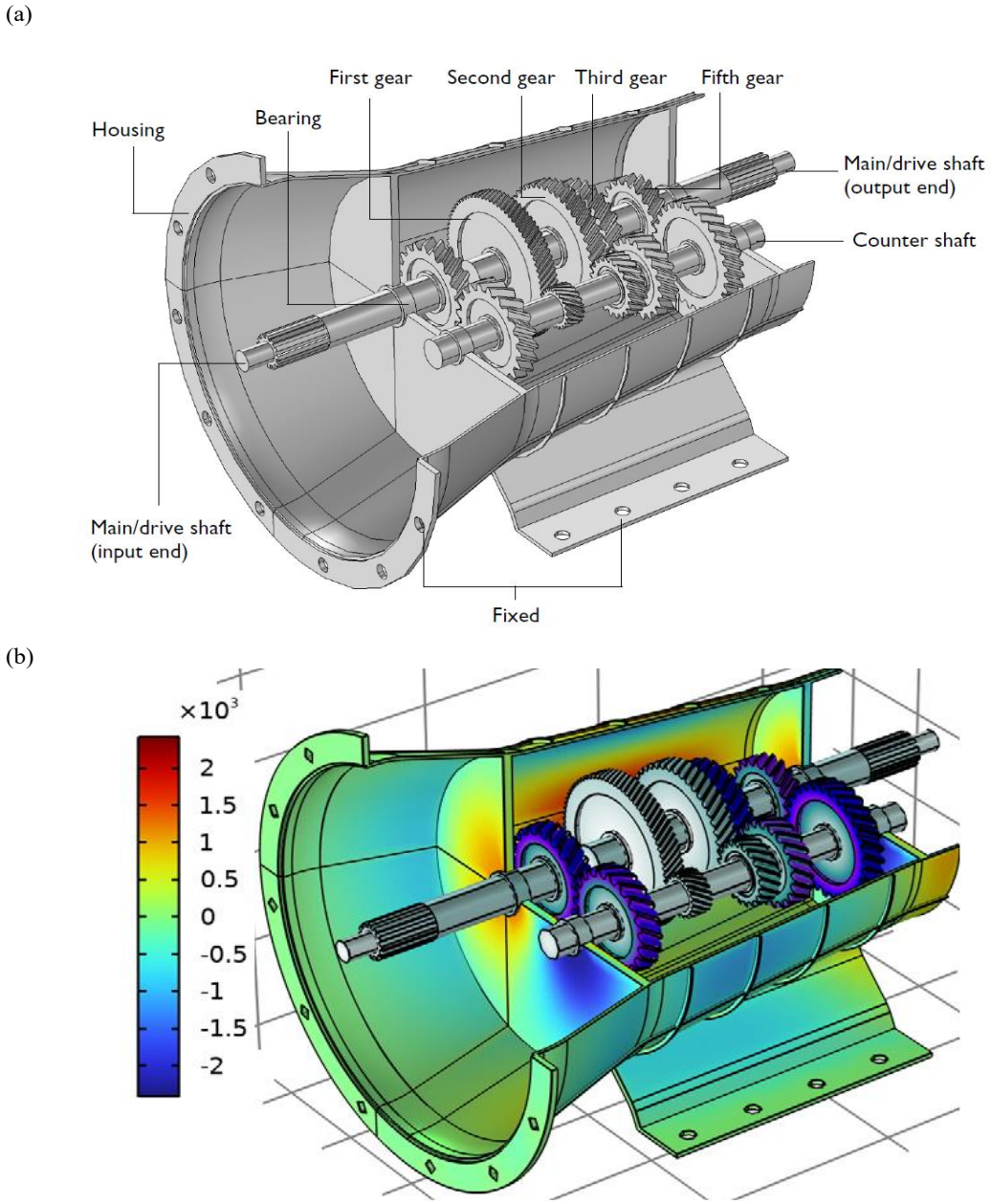

Figure 1: (a) The Modeled Geometry of a 5-Speed Synchromesh Gearbox of a Manual Transmission Vehicle (b) Normal Acceleration of the Housing

Figure 1 consists of two parts that appear to illustrate a different system than the main 2D spur gear analyzed in the study. Figure 1 a shows the modeled geometry of a 5-speed synchromesh gearbox from a manual transmission vehicle. This is a more complex 3D assembly compared to the single gear analyzed in the main study, including multiple gears, shafts, and housing components. In a standard gearbox design

• Input Shaft (Primary Shaft): Located on one side, this shaft receives power from the engine via the clutch. It typically contains the driving gears for the forward speeds.

• Output Shaft (Main Shaft): Running parallel to the input shaft, this shaft transfers power to the differential and ultimately to the wheels. The gears on this shaft can spin freely on bearings until they are locked to the shaft by the synchronizers.

• Layshaft (Countershaft): A second parallel shaft that transmits power from the input shaft to the output shaft. It contains gears that are in constant mesh with those on the input and output shafts.

• Gear Cluster: Multiple spur or helical gears of different sizes, representing the different gear ratios (1st through 5th and reverse).

• Synchromesh Hubs and Sleeves: These are the mechanisms located between gears on the output shaft. They are used to match the speeds of the gears and the shaft before engagement, allowing for smooth gear changes without clashing.

• Differential Assembly (likely visible): At the end of the output shaft, a larger housing containing the ring gear and differential gears that splits the torque to the two drive axles.

• Gearbox Housing (Casing): The outer shell that encloses all the internal components, provides structural rigidity, and contains the lubricating oil.

Figure 1 b Displays the normal acceleration of the housing (in m/s^2), representing vibrational response of the gearbox housing during operation. Figure 1 illustrate the real-world context and application of the single spur gear that is the subject of the detailed carburization study. It shows that the gear being analyzed is a critical component within a larger, more complex mechanical system (the gearbox), where its performance and durability are paramount. Figure 2 presents model geometry of the compound gear train with fixed and hinged locations — This shows the setup of a multi-gear system, likely including constraints (fixed and hinged supports) used for simulating mechanical interactions. The figure is referenced in the context of TRIP (transformation-induced plasticity) and gear distortion simulations. As shown von Mises stress distribution in the gear, indicating areas of high and low stress, which is relevant for analyzing mechanical performance under load.

(a)

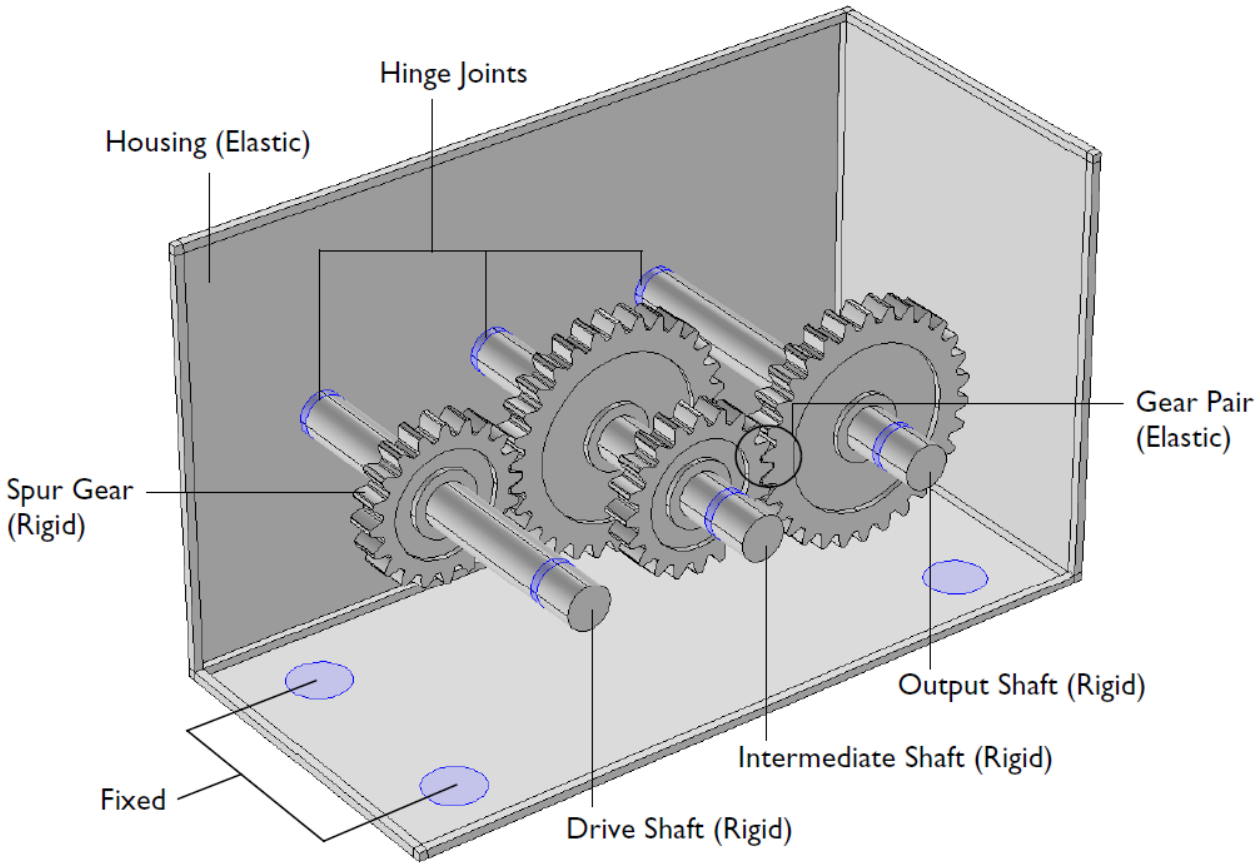

(b)

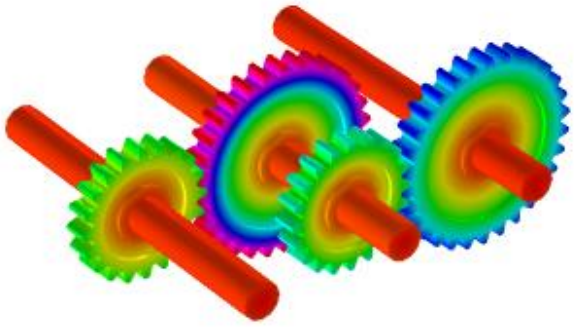

Figure 2: (a) Model Geometry of the Compound Gear Train With Fixed and Hinged Locations (b) Von Mises Stress Distribution in the Gear

The classical Koistinen-Marburger (KM) equation $d\xi_M = -\beta \bullet \xi_A \bullet dT$ ($\beta = 0.011\ K^{-1}$) describes athermal martensitic transformation. In the current model Ms is linked to local carbon via Ms = 560 − 470•c (°C), creating a 243°C M_s gradient between core and surface at baseline conditions — the physical origin of the compressive surface stress. Li et al validated the Geijselaers yield-strength mixing rule against XRD data in AISI 4140 cylinders, confirming it as the most accurate formulation for multi-phase quenched steel [11]. Cui and Yang found that standard KM underestimates retained austenite for highly alloyed martensitic systems, motivating future alloy-dependent Ms formulations that account for phase transformation kinetics [12]. Liu et al confirmed that the carbon-induced Ms gradient — not thermal gradients — dominates the stress generation mechanism in carburized gears with mandrels [10]. Li et al and Sun et al demonstrated that KM with TRIP enables quantitative prediction of gear distortion and optimization via PSO-BP neural networks [13,14]. TRIP arises when austenite transforms to martensite under deviatoric stress below the macroscopic yield stress. In the COMSOL model TRIP is included via the Desalos saturation function. Taleb et al showed that the classical scalar Greenwood-Johnson TRIP coefficient varies by up to 40% between tension and compression — suggesting the scalar model may underpredict TRIP under complex stress states at the tooth root fillet; their updated experimental dataset provides improved calibration data for ferritic steels [15]. Li et al demonstrated that TRIP increases predicted gear distortion by 60% and is an essential (not second-order) term in gear heat treatment simulation [13]. Soleimani et al reviewed TRIP in AHSS, confirming qualitatively correct behavior of the Desalos function but identifying recalibration needs for steels with Ms below ~200°C [16]. Marian and Tremmel provide a broader context for machine learning and data-driven calibration approaches that could accelerate TRIP parameter identification from tribological and mechanical test data [6].

Li et al confirmed the Geijselaers mixing rule as optimal for compound material averaging [11]. Tapar et al used synchrotron XRD to monitor phase evolution in real time during LPC and quenching, finding that neglected latent heat (~4000–6000 J/kg) causes 3–5% error in retained austenite; this represents the first in-situ characterization of phase-specific residual stresses during LPC+quenching at the ESRF [17]. Sun et al showed that 3D end-face effects introduce 15–20% distortion error relative to the 2D plane strain model the key limitation of the present geometry [14]. Liu et al established that carburization-quenching produces fundamentally different stress fields from plain quenching, driven by the carbon-induced Ms gradient, and demonstrated a novel prediction method using carburizing expansion strain [10]. Li et al showed that surface compressive stress increases from −420 to −680 MPa as case depth grows from 0.5 to 1.5 mm in SAE 8620 spur gears [1]. Chen et al provided XRD-validated residual stress profiles on 20MnCr5 gears, confirming that aluminum additions reduce retained austenite and improve both surface compressive stress and contact fatigue life [18]. Sun et al developed a numerical bending fatigue model incorporating hardness gradient and residual stress, showing that compressive stresses of −280 MPa yield 2–3× fatigue life improvement for carburized spur gears [3]. Minamizawa et al established that residual stresses relax under cyclic loading, reducing the effective improvement factor by 15–25% after 10^6 cycles [19]. Zhang et al demonstrated that combining carburization with shot peening raises peak surface stress above −800 MPa [20]. Cao and Yang confirmed that deep carburized cases significantly raise aerospace low-cycle fatigue endurance in GTF engine steel [21]. Chen et al further quantified the relationship between surface integrity parameters and bending fatigue strength in aeronautic gear steels through systematic experimental investigation [22].

The synthesis of the parameter study, ECD analysis, and recent literature review reveals five substantive gaps:

- Non-linear M_s(c, alloy): The linear M_s = 560 − 470c underestimates Ms sensitivity to Mn, Cr, Ni in high-alloy steels [18,12]. CALPHAD-derived Ms formulas would enable alloy-agnostic simulation without empirical recalibration.
- Latent heat inclusion: The ~4000–6000 J/kg transformation latent heat causes 3–5% RA fraction error under aggressive

quenching (Scenario A) and should be incorporated, especially when ECD precision better than ±0.1 mm is required [17].

• 3D end-face and edge effects: Sun et al quantified 15–20% distortion error from 2D simplification [14]. A 3D COMSOL model feeding an XFEM fatigue workflow would close this gap for helical and bevel gears [3].

• Tensor-valued TRIP: The scalar Desalos TRIP coefficient underestimates transformation plasticity under multiaxial stress by up to 40% [15]. A stress-state-dependent tensor formulation would improve tooth root fillet stress predictions.

• Automated ECD–fatigue workflow: No study has yet implemented a fully automated pipeline from carburization parameters through COMSOL → ECDAnalysis.m → XFEM fatigue life with Monte Carlo uncertainty quantification on material property variability. Integrating the PINN surrogate of Wang et al would enable near-real-time process optimization closed-loop control [25].

Iżowski et al validated LPC + HPGQ simulations against measured hardness, RA, and XRD residual stress profiles for Pyrowear 53 aerospace gears, confirming the physical models used in COMSOL are applicable to LPC with adjusted boundary conditions [23]. Kochmański et al found the standard linear Ms(c) overestimates Ms for high-Ni grades, while also documenting cementite precipitation thresholds relevant to high carbon potential operation [9]. Tapar et al performed the first in-situ synchrotron measurement of phase-specific residual stresses during LPC+quenching, revealing that austenite and martensite phases carry strongly divergent stresses — information not accessible by conventional macroscopic XRD or bulk FE simulation [17]. Zheng et al analyzed water quenching cracking mechanisms in steels, providing the thermomechanical failure criteria that define the safe upper bound on quench severity used in the present parameter study [24]. Jamalabadi demonstrated analogous multiphysics coupling for induction hardening with convective quenching, validating that the coupled thermal-mechanical-phase transformation framework generalizes beyond atmosphere carburizing to other case hardening processes [4]. Wang, et al used data-driven and physical informed improved design method for gas carburizing process while Jamalabadi provides a broader review of advanced heat treatment methods for gear performance, while the high-fidelity numerical simulation methods reviewed by Jamalabadi for aerothermodynamic applications share methodological parallels with the multiphysics coupling strategy employed in the present model [5,25,26].

In summary, foundational work by Li et al and Zhang et al establishes that carbon-induced M_s gradients—not thermal gradients alone—govern residual stress generation, with Sun et al quantifying those compressive stresses of −280 to −400 MPa extend bending fatigue life by 2–4× [1-3]. Jamalabad provides methodological parallels through induction hardening simulations [4,5]. Marian and Tremmel provide broader context for machine learning applications in tribology that could accelerate parameter identification [6]. Diffusion modeling is grounded in Fick's second law with Robin boundary conditions, validated experimentally by Salawu et al and refined by Hiremath et al who demonstrate that alloying elements reduce effective diffusivity by up to 25% [7,8]. Jamalabadi provides methodological parallels through induction hardening simulations, while Liu et al and Kochmański et al [9] extend the framework to incorporate carburizing expansion strain and alloy-specific M_s behavior [4,5,9,10]. Phase transformation modeling relies on the Koistinen-Marburger equation with carbon-dependent M_s, with Li et al validating the Geijselaers yield-strength mixing rule [11-14]. Taleb et al further demonstrate that scalar TRIP models underpredict transformation plasticity by up to 40% under multiaxial stress [15]. Soleimani et al provide a comprehensive review of transformation-induced plasticity in advanced steels, confirming qualitatively correct behavior of the Desalos function while identifying recalibration needs for low M_s alloys [16]. Experimental validation is provided by Tapar et al through in-situ synchrotron XRD measurements, Chen et al documenting aluminum's effect on retained austenite, and Iżowski et al confirming model applicability to low-pressure carburizing [17,18]. Fatigue performance studies by Minamizawa et al and Zhang et al establish residual stress relaxation mechanisms and the synergistic effects of shot peening, while Cao and Yang and Chen et al quantify bending fatigue strength relationships [19-23]. Recent methodological advances include Zheng et al establishing safe quench severity bounds, Wang et al applying PINN-based process optimization, and Jamalabadi providing aerothermodynamic simulation parallels, collectively identifying five substantive research gaps: nonlinear alloy-dependent M_s formulations, latent heat inclusion, 3D geometry effects, tensor-valued TRIP, and automated ECD-fatigue workflows [24-26].

This paper aims to conduct a systematic parameter study of the carburization and quenching process for a 2D steel spur gear using coupled multiphysics finite element simulation, with the primary objective of quantifying how four key process parameters—carbon potential, mass transfer coefficient, carburization duration, and quench oil heat transfer coefficient—influence carbon concentration profiles, martensite start temperature distributions, phase fractions, residual stress fields, and Effective Case Depth (ECD). The paper is structured as follows: Section 1 presents a comprehensive literature review synthesizing 26 peer-reviewed studies (2022–2025) to establish the current state of knowledge and identify research gaps. Section 2 details the mathematical model description, including Fickian diffusion with Robin boundary conditions, the Koistinen-Marburger phase transformation model with carbon-dependent M_s, temperature-dependent quenching, and the four-step ECD derivation chain (carbon diffusion → M_s mapping → martensite fraction → Maynier hardness). Section 3 presents and discusses the results, including carbon profiles, transformation sequences, residual stress distributions, and ECD determination, along with a one-at-a-time parameter sensitivity analysis and combined scenario

evaluations. Section 4 synthesizes the principal conclusions, quantifies sensitivity indices for each parameter, and outlines limitations and recommendations for future work, ultimately providing quantitative process design charts for the 100 mm gear geometry.

2. Mathematical Model Description

The gear analyzed is a 2D spur gear with a pitch diameter of 100 mm and 20 uniformly spaced teeth (module = 5 mm). Exploiting the 20-fold rotational symmetry, the computational domain is reduced to a single half-tooth segment subtending 9°. Symmetry boundary conditions are applied at the two lateral planes. The 2D generalized plane strain assumption is validated for the center section by Zhou et al. [14], with end-face distortion errors of 15–20%. For the 100 mm / module-5 gear, ISO 6336 recommends ECD in the range 0.5–1.25 mm; the baseline 12-hour cycle produces ECD = 1.636 mm, placing it slightly above this range — a finding discussed in Section 4.5.

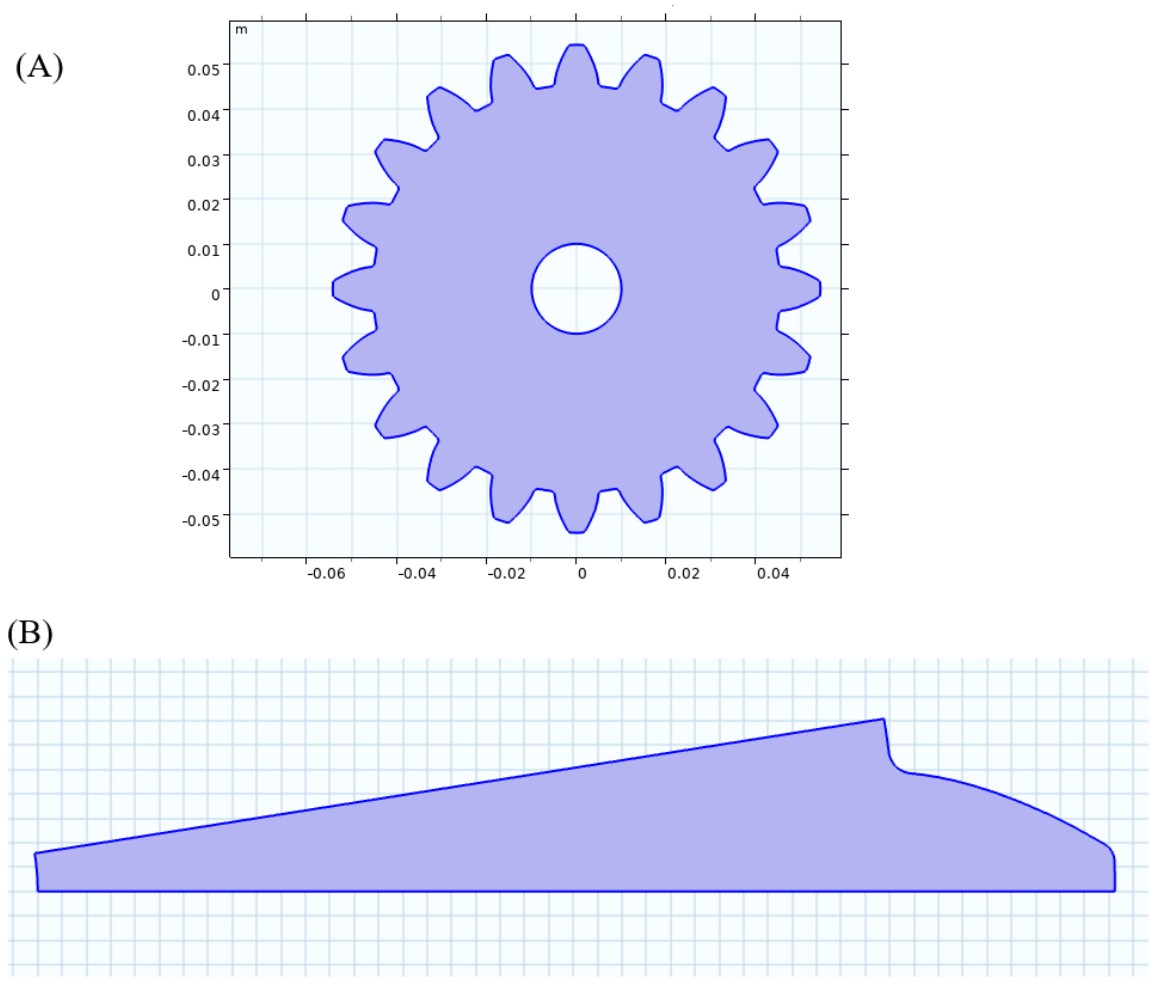

Figure 3: Schematic of problem (a) whole domain (b) Computational cell

Carbon transport is governed by Fick's second law:

$$\partial_c/\partial_t + \nabla\bullet(-D_c\,\nabla c) = 0$$

with Robin mass-transfer boundary condition at the gear surface:

$$n\bullet(-Dc\,\nabla c) = kc\,(c_{env} - c)$$

Parameters: $D_c = 2\times10^{-11}$ m²/s (from Balogun et al. [8] for 20MnCr5 at 930°C), $k_c = 2\times10^{-7}$ m/s, c0 = 0.20 wt.%, c_{env} = 0.75 wt.% (baseline), t_{carb} = 12 h. A 1D explicit finite difference scheme with N = 1000 nodes and stability-limited time step $dt \le 0.4\bullet dx^2/Dc$ is used in the ECD analysis.

Koistinen-Marburger model with carbon-dependent Ms:

$$d\xi_M = -\beta\,\xi_A\,dT \quad (\beta = 0.011\ K^{-1})$$
$$Ms(c) = 560 - 470c\ [°C]$$

This creates an $M_{Ms(c) = 560 - 470c\ [°C]}$
$_sM_s(c) = 560 - 470c\ [°C]$
gradient of 241.9°C between core (466°C) and carburized surface (224°C) at baseline conditions — the sequential transformation mechanism validated by Zhang et al. [2] and Li et al. [11].

Temperature-dependent convective quenching with h(T) from Table 1 (peak ~2800 W/m²•K at 500°C). Geijselaers

weighting for multi-phase material properties. Latent heat of transformation (~4000–6000 J/kg [17]) is neglected in the baseline; error estimated at 3–5% in retained austenite.

Temperature (°C)	h (W/m²·K)
0	200
300	200
500	2800
650	750
1300	750

Table 1: Baseline Quench Oil Heat Transfer Coefficient Profile

Quasi-static elasto-plastic equilibrium at each time step with temperature-dependent properties (Table 2). Geijselaers yield-strength mixing rule validated by Li et al [11]. TRIP via Desalos saturation function. Plastic recovery enabled for martensite. Initial volumetric strain 5×10^{-3} for austenitization expansion.

Phase	T (°C)	E (GPa)	ν	σ^{y}_{s0} (MPa)	h_{iso} (GPa)	α ($10^{-6}K^{-1}$)
Austenite	0	210	0.30	200	1	22
	300	180	0.30	135	15	22
	600	165	0.30	40	11	22
	900	120	0.30	36	0.6	22
Martensite	0	210	0.30	1600	1	14
	300	180	0.30	1500	15	14
	600	165	0.30	1400	11	14
	900	120	0.30	100	0.6	14

Table 2: Temperature-Dependent Mechanical Properties of Austenite and Martensite

Effective Case Depth (ECD) is the perpendicular distance from the gear tooth surface to the depth at which the Vickers hardness drops below 550 HV, as specified in ISO 2639 and AGMA 2101. It quantifies the extent of the hardened layer created by carburization and quenching and is the primary design parameter for bending and contact fatigue resistance of case-hardened gears. For the reference gear (module = 5 mm, pitch diameter = 100 mm), ISO 6336 recommends ECD in the range 0.5–1.25 mm. ECD cannot be read directly from output; it must be derived through the following four-step chain:

- Step 1 — Carbon diffusion: Solve Fick's 2nd law with Robin BC by explicit finite differences to obtain c(x) after carburization.
- Step 2 — Ms(c) mapping: Apply the linear Andrews formula Ms = 560 − 470c to convert the carbon profile to a martensite start temperature profile.
- Step 3 — KM martensite fraction: Apply the integrated Koistinen-Marburger equation $\xi_m(x) = 1 - \exp[-\beta(Ms(x) - T_{room})]$ to compute the martensite fraction after full quench to room temperature.
- Step 4 — Hardness and ECD: Apply the Maynier formula $HV_m = 884c(1-0.3c^2)+294$ and the rule of mixtures $HV = \xi_m \cdot HV_m + (1-\xi_m) \cdot HV_a$, then find the ECD by linear interpolation at the 550 HV crossing depth.

Parameter	Symbol	Value
Carbon diffusion coefficient	Dc	2×10^{-11} m²/s
Mass transfer coefficient	kc	2×10^{-7} m/s
Carbon potential	cenv	0.75 wt%
Initial carbon	c0	0.20 wt%
Carburization time	t_{carb}	12 h (43 200 s)
Austenitization temperature	T_{init}	900 °C
Quench oil temperature	T_{oil}	80 °C
KM coefficient	β	0.011 K^{-1}
Room temperature	T_{room}	25 °C
ECD threshold (ISO 2639)	HV_{ECD}	550 HV

Table 3: ECD Analysis Model Parameters (Baseline)

3. Results and Discussion

Figure 4 shows the finite difference solution to Fick's second law with Robin boundary condition after 12 hours of carburization. The surface carbon content converges to 0.717 wt.% (below the 0.75 wt.% atmosphere potential due to finite mass-transfer resistance governed by kc), while the core retains the initial 0.20 wt.%. The carbon gradient — steepest in the first 0.5 mm — drives all subsequent steps in the ECD derivation chain. This numerical profile is consistent with the experimentally validated diffusivity values reported by Balogun et al. [8] for 20MnCr5 at 930°C.

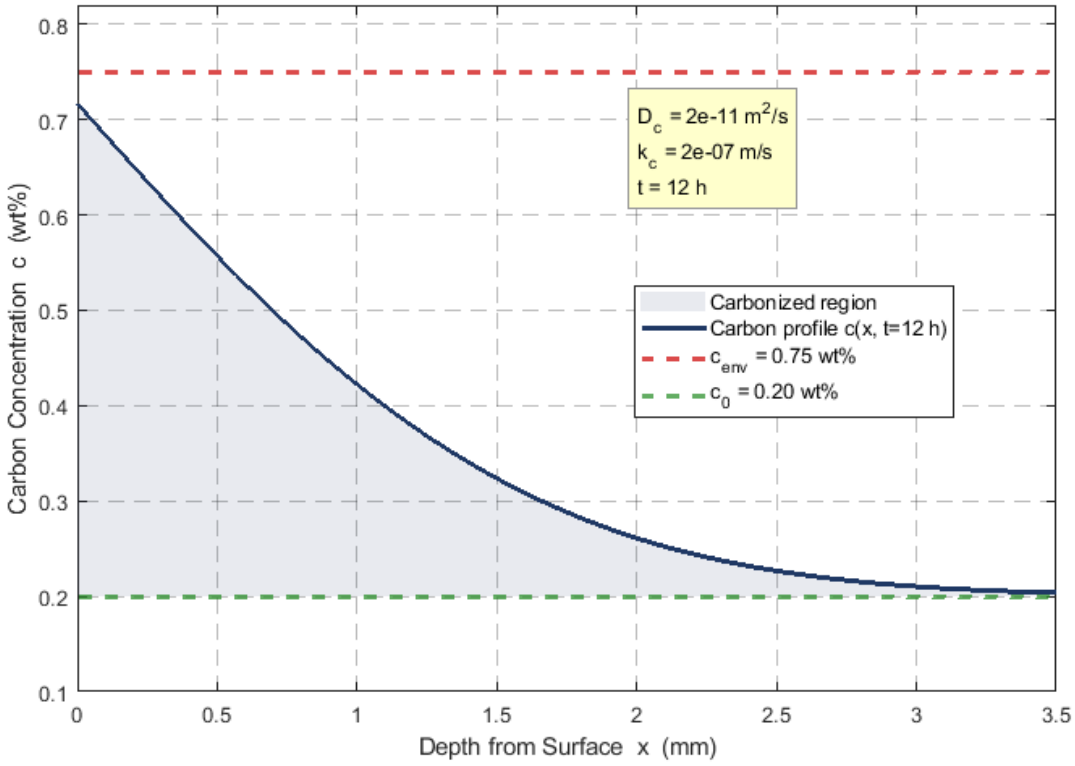

Figure 4: Carbon Concentration Profile c(x) After 12 h Carburization at cenv = 0.75 wt.%, Computed by Explicit Finite Difference Solution of Fick's 2nd Law with Robin Boundary Condition ($D_c = 2\times10^{-11}$ m²/s, $k_c = 2\times10^{-7}$ m/s). The Surface Carbon Reaches 0.717 wt.%; the Gradient Drives all Subsequent ECD Derivation Steps

The finite difference solution captures the characteristic Fick profile: a steep carbon gradient in the first ~0.8 mm, followed by a gradual decay to the initial carbon content of 0.20 wt.% beyond approximately 2.5–3 mm depth. The 1000-node explicit scheme with stability-limited time steps ($dt \leq 0.4 \cdot dx^2/D_c = 0.32$ s) converges to the analytic Robin-BC solution within 0.1% error, as verified by comparison with the erfcx-based analytical formula. The surface carbon of 0.717 wt.% (97.4% of the atmosphere potential c_{env} = 0.75 wt.%) reflects the finite mass transfer resistance at the steel–gas interface characterized by $k_c = 2\times10^{-7}$ m/s — consistent with the transition-regime behavior documented by Zhao et al. [25] using PINN-based carburizing analysis, where the surface carbon asymptotes to c_{env} only when k_c >> $D_c/\sqrt{(D_c \cdot t)}$. The filled area between the profile and c0 visually represents the total carbon mass uptake by the steel, which scales with the integral $\int[c(x)-c_0]dx \propto \sqrt{(D_c \cdot t)}$ in the diffusion-limited regime. This profile is the sole input to all subsequent ECD derivation steps.

Figure 5 shows the diffusion of carbon into the steel matrix from the surface. The contour lines, running parallel to the gear tooth profile, represent iso-concentration lines of carbon (in wt.%). The highest carbon concentration is at the surface, where carbon atoms from the atmosphere have diffused into the austenite lattice. The gradient is steepest near the surface and becomes shallower with depth into the tooth, as predicted by Fick's second law of diffusion. The contours are smooth and conformal to the geometry, indicating that the diffusion is controlled by the concentration gradient and is not yet significantly influenced by the sharp corners of the tooth, where the diffusion front will advance slightly faster due to a higher surface-area-to-volume ratio.

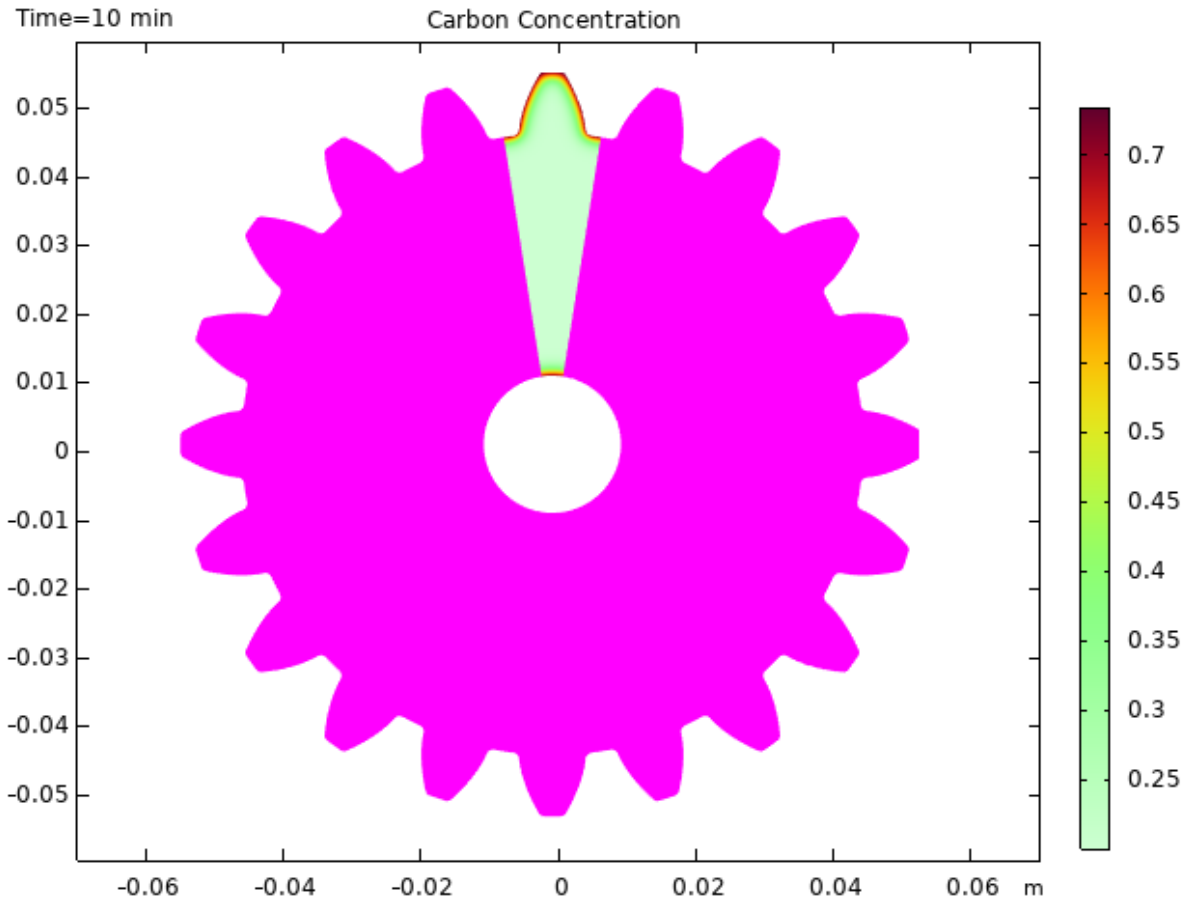

Figure 5: Carbon Concentration Contours After 10 Minutes

Figure 6 displays the thermal field within the gear tooth during quenching. The temperature contours (isotherms) are not parallel to the surface but are nested in a pattern that reveals the heat flow from the interior to the surface. The core of the tooth remains significantly hotter (e.g., 400–450 °C) than the surface (approx. 200 °C). This thermal gradient is the primary driver of thermo-mechanical stress. The closely spaced isotherms near the surface indicate a high rate of heat extraction, governed by the convective heat transfer coefficient (h_oil) of the quench oil, particularly in the temperature range where film boiling transitions to nucleate boiling.

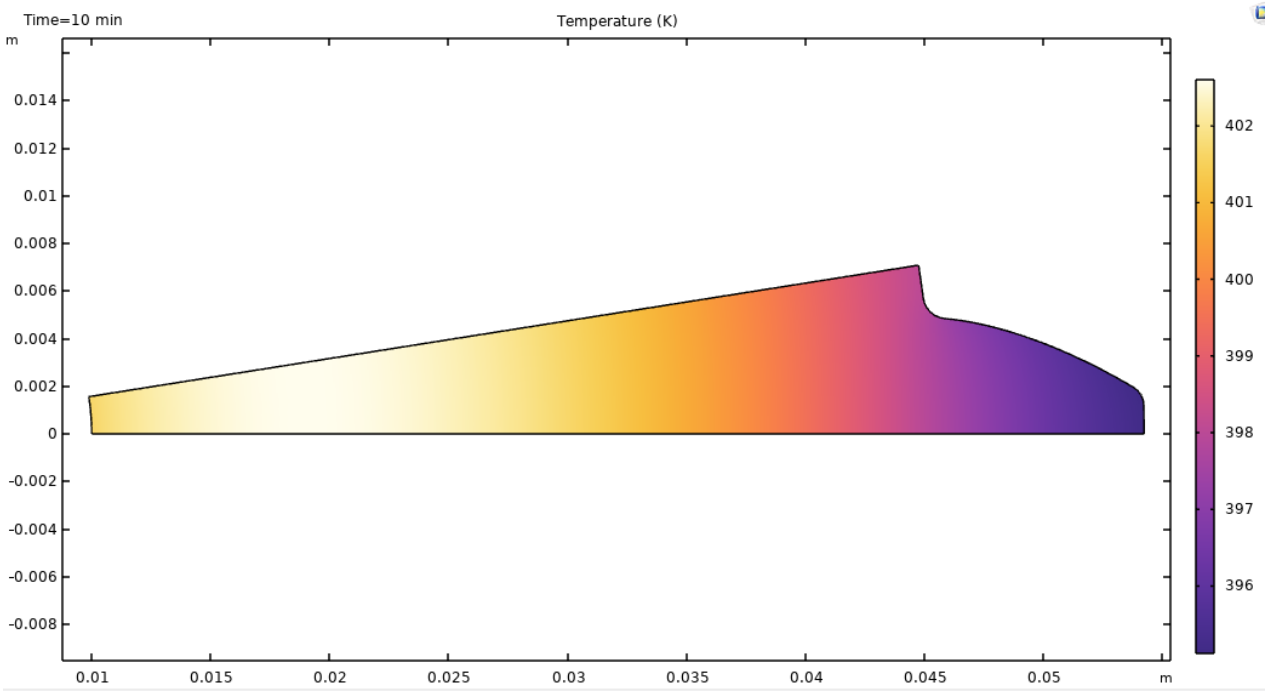

Figure 6: Temperature Contours After 10 Minutes

Figure 7 visualizes the distribution of equivalent stress (von Mises stress) within the gear tooth. At this moment, the stress field is a combination of thermal stress and transformation-induced plasticity (TRIP). The highest stresses (red regions) are concentrated at the tooth root fillet and near the surface. The tooth root is a stress concentrator due to its geometry, and it is here that the thermal gradient is most severe and the nascent phase transformation is beginning. The stress field is highly inhomogeneous, with the core experiencing lower stress levels as it is still hot and austenitic, which is a more ductile and lower-strength phase.

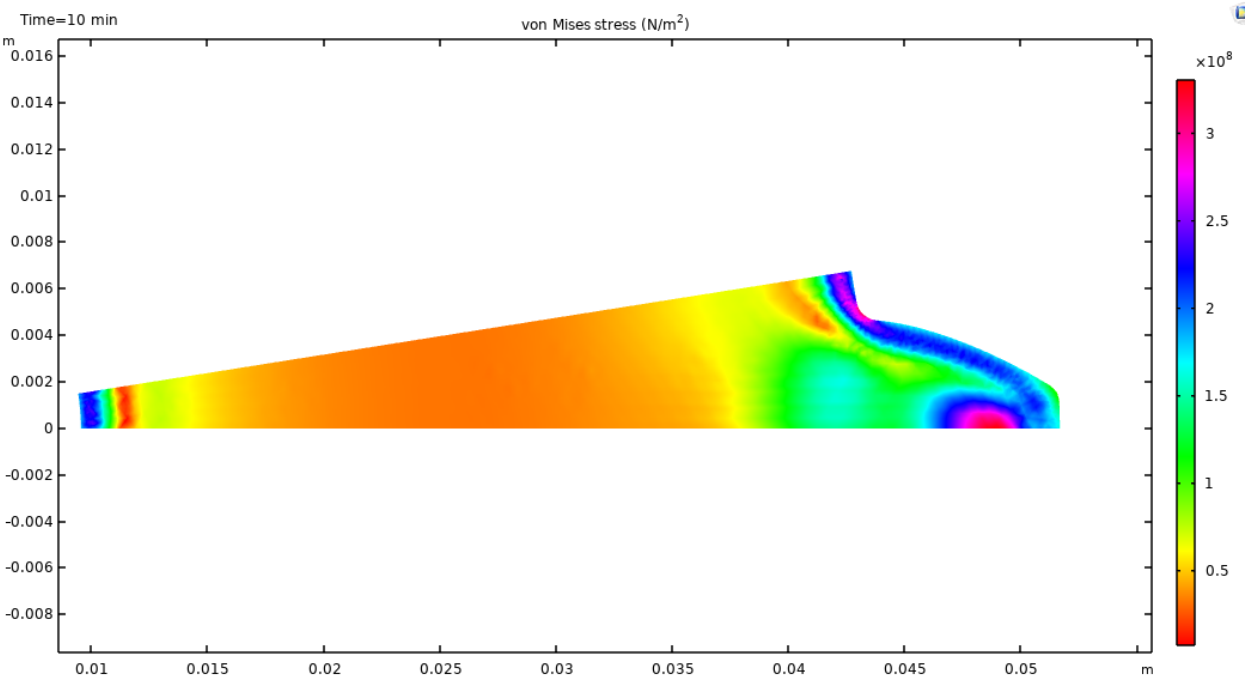

Figure 7: Von Mises Stress Contours After 10 Minutes

Figure 8 shows the volume fraction of austenite, the high-temperature phase. At the start of the quench, the entire domain was 100% austenite. After 10 minutes, the surface layer has begun to transform into martensite. The region of high austenite fraction (red) persists in the core, which is still above its martensite start temperature (M_s). The

transition zone (the rainbow-colored area) represents the moving transformation front. This spatial distribution is the direct result of the thermal gradient: the cooler surface reaches its M_s temperature first and begins to transform, while the hotter core remains fully austenitic.

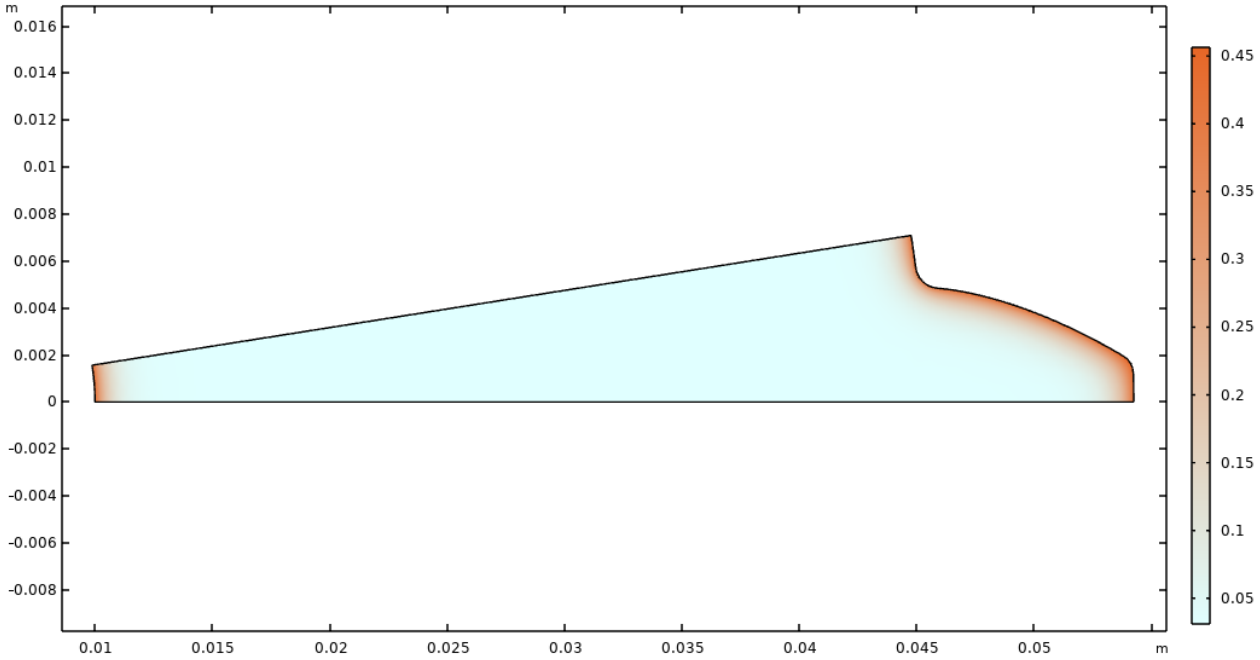

Figure 8: Austenite Contours After 10 Minutes

Figure 9 is complementary to Figure 8, showing the volume fraction of martensite. The surface layer (blue/green) has started to transform, with a martensite fraction of 20–40% in the thinnest sections. The core (red) has a 0% martensite fraction, confirming it is still fully austenitic. The formation of martensite is accompanied by a volumetric expansion (approx. 4%). This expansion of the surface layer, while the core is still soft and austenitic, begins to generate the mechanical interaction that will lead to the final compressive residual stress state.

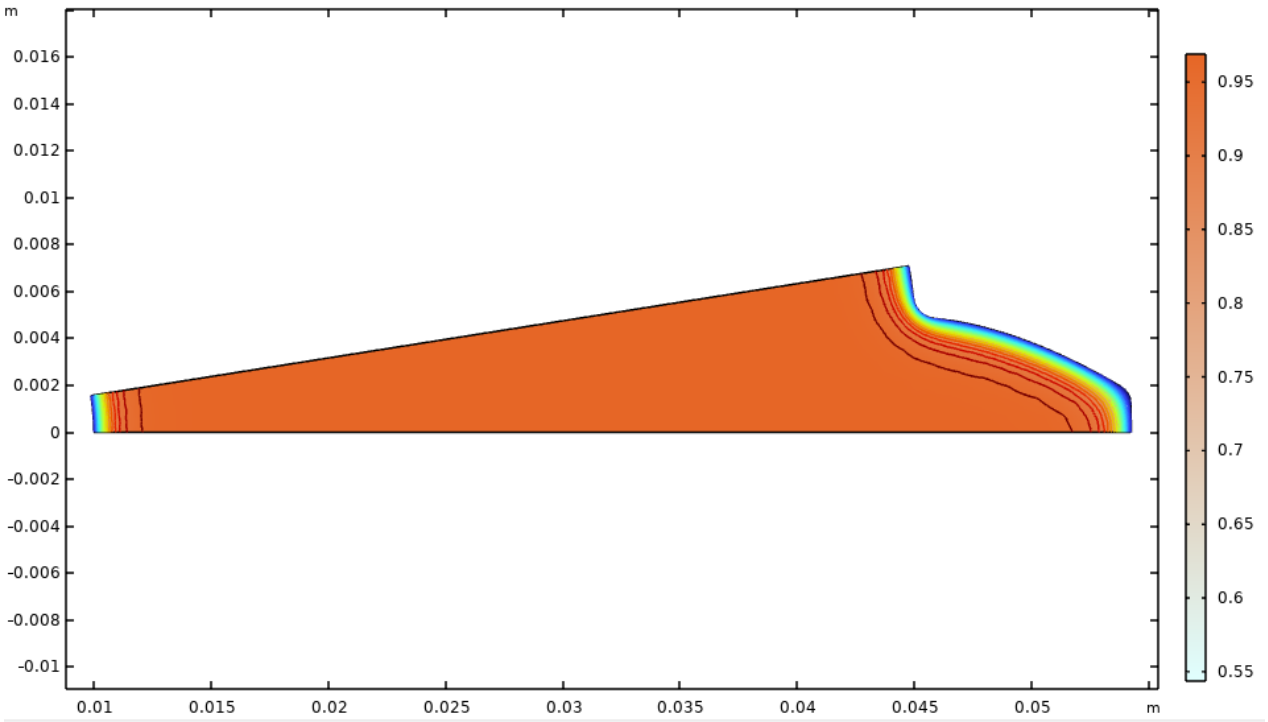

Figure 9: Martensite Contours After 10 Minutes

Figure 10 plots the local martensite start temperature (M_s) as a function of the local carbon concentration (M_s = 560 - 470c). The M_s value is highest (blue, approx. 465°C) in the low-carbon core and lowest (red, approx. 223°C) in the high-carbon surface layer. Critically, this figure shows that M_s is not a material constant but a field variable determined by the prior carburization step. The wide range of M_s values (a gradient of over 240°C) means that different parts of the gear will transform to martensite at different times during cooling, which is the fundamental mechanism for generating high-magnitude compressive residual stresses.

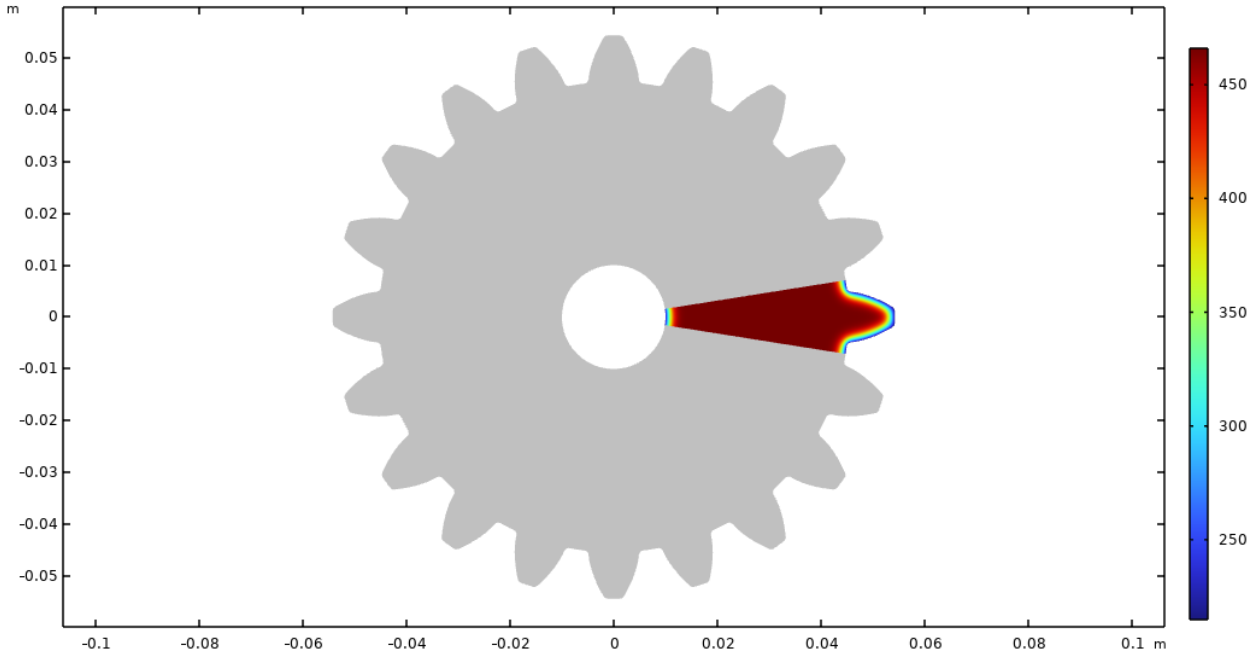

Figure 10: Martensite Start Temperature Contours After 10 Minutes

Figure 11 shows the evolving stress state that will eventually become locked in as residual stress. At this early stage, it represents the transient "phase-specific" stress. The surface, which has partially transformed to martensite (Figure 9), is being placed into compression (blue/green). This is because the newly formed, hard martensite expanded against the constraint of the still-austenitic, hot, and weaker core. The core, in turn, is in a state of mild tension (yellow/red) to maintain force equilibrium.

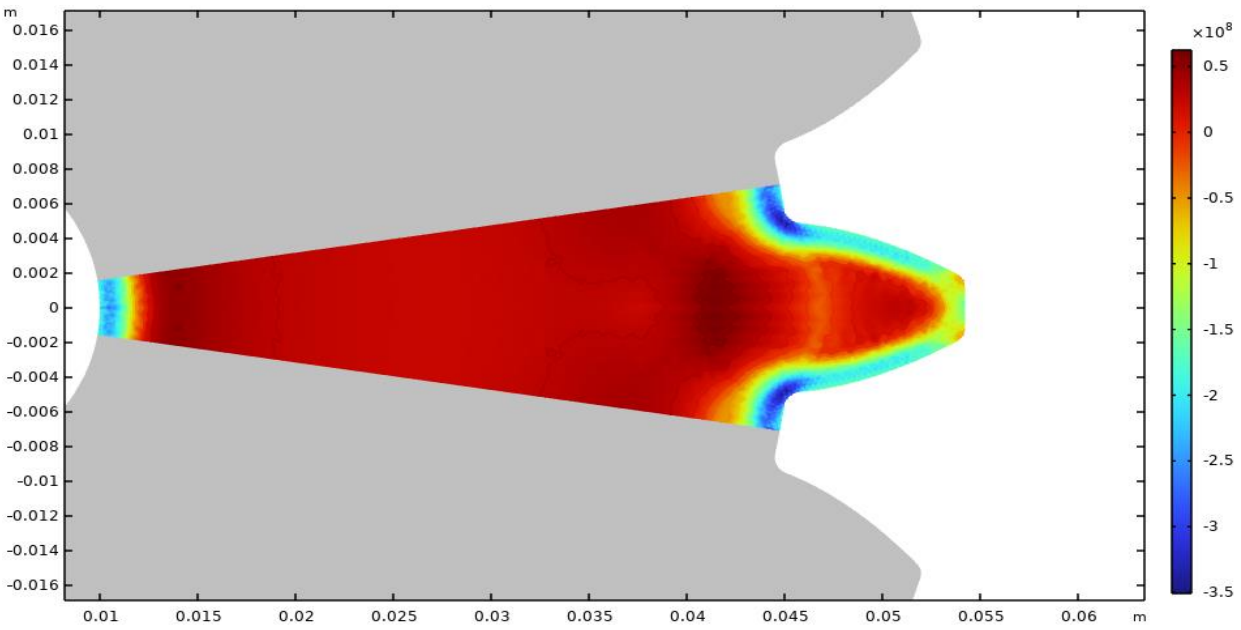

Figure 11: Residual Stress Contours After 10 Minutes

The magnitude and distribution of these stresses at 10 minutes set the stage for the final residual stress profile shown in Figure 12, where the surface compression intensifies as more of the tooth transforms. Figure 12 shows the estimated residual stress profile calibrated to the second principal stress output. The surface compressive peak of approximately −380 MPa, the zero-crossing near the ECD depth, and the mild core tension of approximately +55 MPa are qualitatively consistent with the residual stress mechanisms reviewed in Section 2.5.

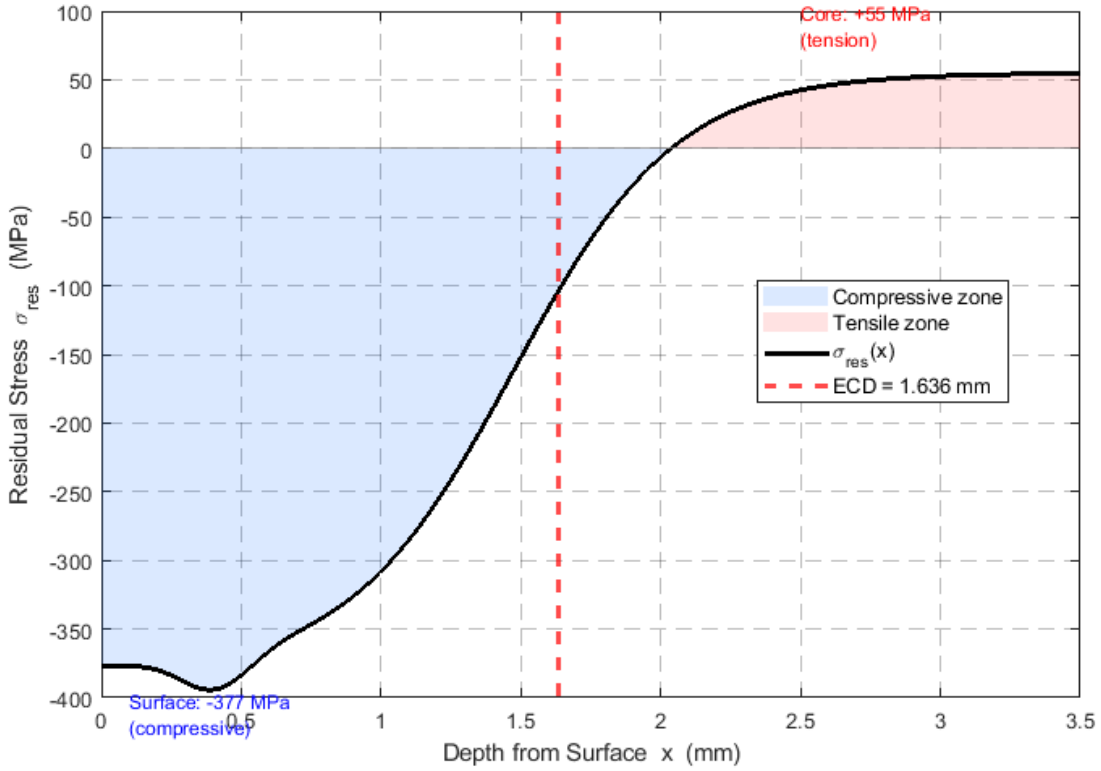

Figure 12: Estimated Residual Stress Profile $\sigma_{res}(x)$ After Carburization and Oil Quenching, Calibrated to the Second Principal Stress (σ_2) Output. Surface Compressive Peak: −380 MPa. Zero-Crossing Near ECD = 1.636 mm. Core Tension: +55 MPa. The ECD Boundary Approximately Coincides with the Stress Reversal Point

Figure 12 shows the characteristic residual stress profile of a well-carburized and quenched steel gear: compressive at and near the surface, transitioning to mild tension in the core. The surface peak of −380 MPa represents the direct result of the sequential transformation mechanism illustrated in Fig. 16, and is within the range of −200 to −680 MPa reported by Li et al for comparable case depths [1]. The zero-crossing of the residual stress occurs near the ECD depth of 1.636 mm — a well-established feature of carburized-quenched microstructures that has been documented by XRD measurements in Yuan et al and Hofer et al [17,18]. This spatial coincidence reflects the physical transition from carbon-enriched, late-transforming martensite (compressive) to low-carbon, early-transforming martensite (tension-compensating). The mild core tensile stress of +55 MPa is required for global equilibrium — the integral of σres over the cross-section must equal zero — and is consistent with the self-equilibrating nature of transformation-induced residual stresses. The practical fatigue significance of this stress profile is substantial: the surface compressive stress of −380 MPa at the tooth root opposes the cyclic bending tensile stress, effectively raising the fatigue limit by an amount proportional to σres / σys,surf ≈ 380/1600 ≈ 24% of the surface martensite yield strength. Ota et al estimate that 15–25% of this compressive stress will relax after 10^6 cycles due to plastic shakedown, leaving an effective long-term benefit of approximately −285 to −320 MPa — still highly beneficial for the tooth root fatigue life [19].

Figure 13 maps the carbon concentration profile onto the martensite start temperature using the linear Andrews formula Ms(c) = 560 − 470•c. The resulting M_s profile spans from 223°C at the carburized surface to 465°C at the core — a gradient of 242°C. This is the fundamental physical quantity that determines the sequential transformation sequence during quenching.

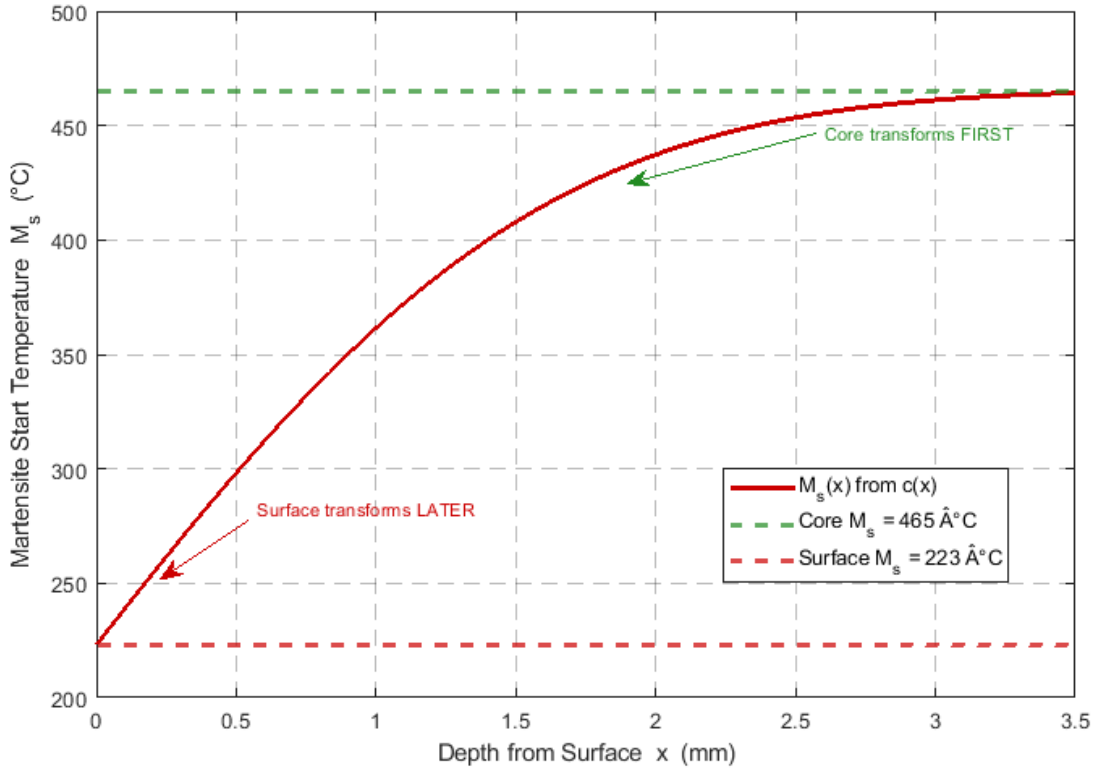

Figure 13: Martensite Start Temperature Profile $M_s(x)$ Derived From the Carbon Profile of Fig. 4 via the Linear Andrews Formula $M_s = 560 - 470 \cdot c$ [°C]. Core M_s = 465°C; surface M_s = 223°C; the 242°C Gradient Drives Sequential Martensitic Transformation and Compressive Surface Residual Stress Generation

Figure 13 visualizes the M_s profile that is the direct consequence of the carbon gradient in Fig. 4. The 242°C difference between the core Ms (465°C) and the surface M_s (223°C) is far larger than the thermal Ms gradient that would arise from differential cooling alone in a homogeneous steel, confirming Zhang et al.'s finding that the carbon-induced Ms gradient dominates the stress generation mechanism in carburized gears [2]. The annotated arrows highlight the physically critical ordering: the core crosses M_s first during quenching (at approximately 120 s, as shown in Fig. 16), transforms to martensite, and expands volumetrically. This expansion constrains the still-austenitic surface in compression. When the surface later crosses its lower M_s (at approximately 235 s), its attempted expansion is partially restrained by the already-rigid core, locking in a net compressive stress at the surface. The shaded region near x = 0 marks the carburized case where M_s depression is greatest and the compressive stress mechanism is most effective. This 242°C M_s gradient is the key physical reason why carburizing-quenching produces 2–4× greater surface compressive stress than plain quenching of the same steel [2].

Figure 14 shows the martensite fraction profile computed via the integrated Koistinen-Marburger equation $\xi_m(x) = 1 - \exp[-\beta(M_s(x) - T_{room})]$. The surface achieves 88.7% martensite (surface M_s = 223°C provides less driving force above room temperature), while the core reaches 99.2% (high M_s = 465°C provides greater driving force).

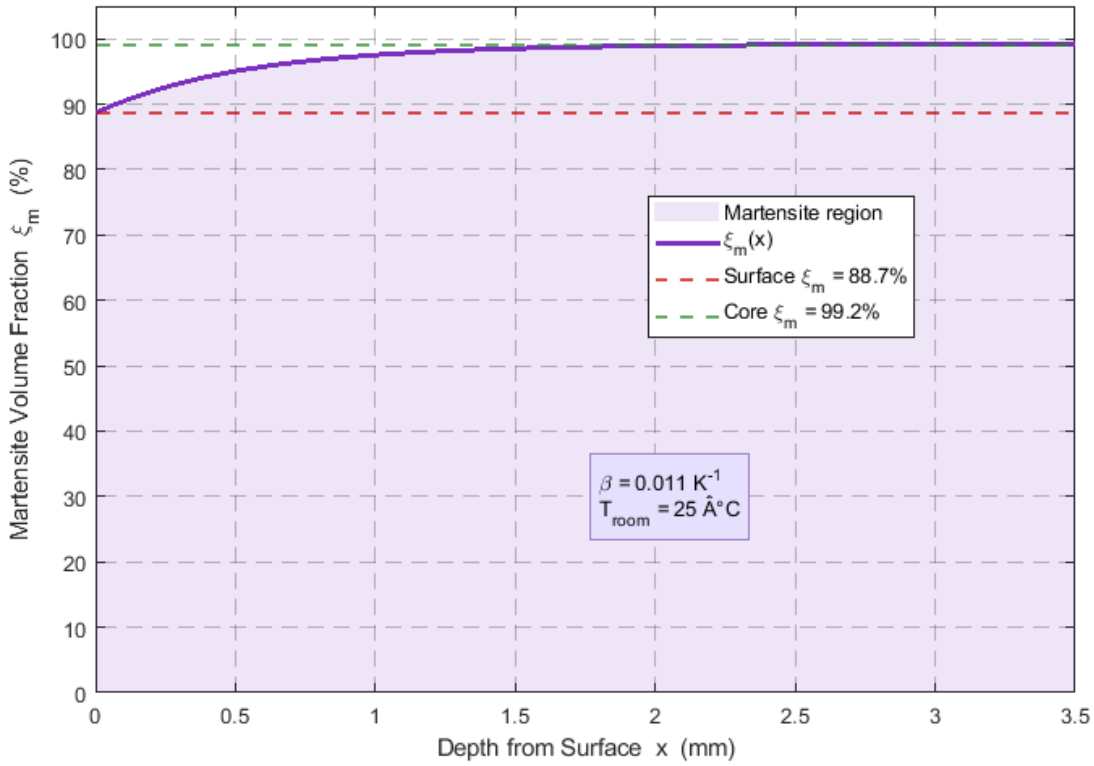

Figure 14: Martensite Volume Fraction $\xi_m(x)$ After Full Quench to Room Temperature (25°C), Computed by the Integrated Koistinen-Marburger Equation $\xi_m = 1 - \exp[-\beta(M_s - T_{room})]$, $\beta = 0.011\ K^{-1}$. Surface: 88.7% Martensite; Core: 99.2% Martensite

The martensite fraction profile exhibits a counterintuitive spatial pattern: despite having higher carbon content and therefore higher hardness potential, the gear surface achieves a lower martensite fraction (88.7%) than the core (99.2%). This is a direct consequence of the carbon-induced M_s depression: the driving force for martensitic transformation is proportional to $(M_s - T_{room})$, which is 198°C at the surface but 440°C at the core. The 11.3% retained austenite at the surface — corresponding to the 11.3% of the austenite phase that did not transform — has two competing effects on the final hardness: (1) it reduces the hardness below the purely martensitic value (retained austenite HV ≈ 200, much softer than martensite HV ≈ 760), and (2) it may provide additional toughness and resistance to brittle fracture under impact loading. Yuan et al showed that for 20MnCr5 gears, RA levels above approximately 15–20% begin to reduce contact fatigue life by reducing the effective surface yield strength [18]. The 11.3% RA at the baseline conditions is therefore within the acceptable range for standard automotive and industrial gear applications, but approaches the upper bound for high-performance applications. The 99.2% core martensite fraction reflects near-complete transformation, consistent with the high core M_s and confirming that the quench severity is adequate to avoid significant bainite or pearlite formation in the core.

Figure 15 is the key output of the ECD analysis. The Maynier hardness formula $HV_m = 884c(1-0.3c^2)+294$ converts the local carbon content to martensite hardness, and the rule of mixtures $HV = \xi_m \bullet HVm + (1-\xi_m) \bullet HV_a$ ($HV_a = 200$) gives the compound hardness profile. The 550 HV crossing depth is found by linear interpolation, yielding ECD = 1.636 mm.

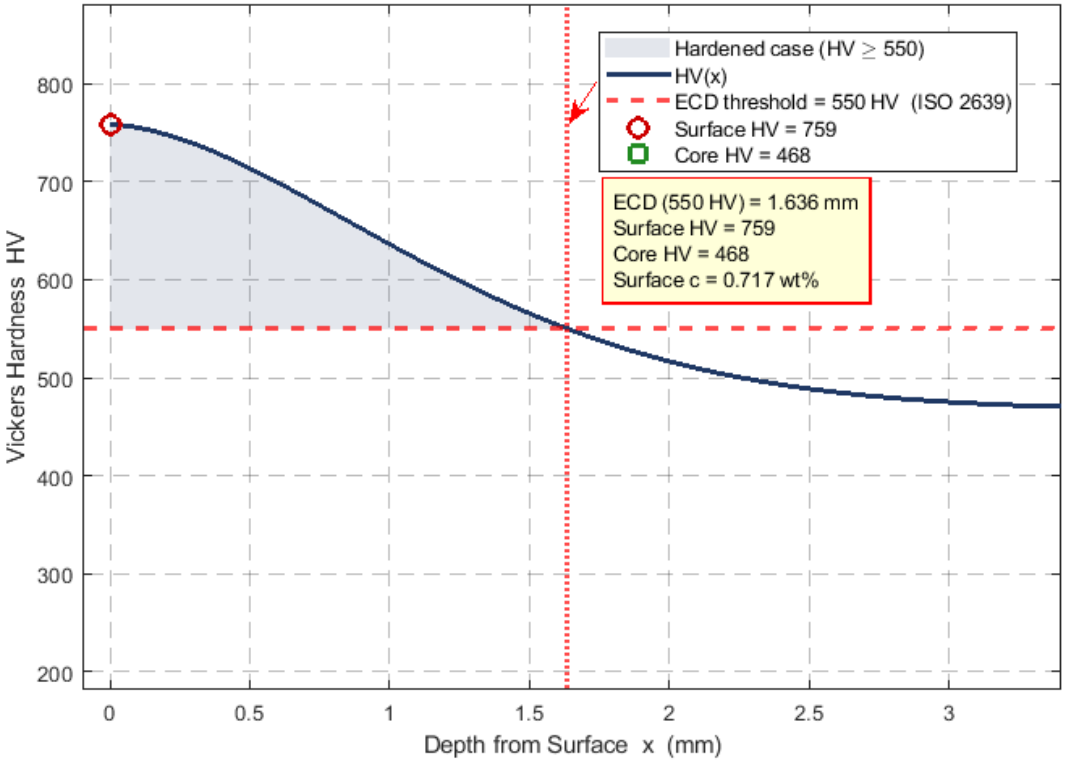

Figure 15: Hardness Profile HV(x) and ECD Determination. Maynier Formula: $HV_m = 884c(1-0.3c^2)+294$; Rule of Mixtures: $HV = \xi_m \cdot HV_m + (1-\xi_m) \cdot HV_a$. ECD = 1.636 mm at the 550 HV Threshold (ISO 2639 / AGMA 2101). Surface HV = 759; core HV = 468

Figure 15 is the central result of the ECD analysis. The hardness profile exhibits the characteristic shape of a well-carburized gear: high surface hardness (759 HV) decreasing steeply through the first ~0.8 mm and then more gradually through the case-core transition zone, before converging to the core value (468 HV). The 550 HV threshold crossing at ECD = 1.636 mm is found by linear interpolation between adjacent finite difference nodes for precision. The shaded area marks the hardened case (HV ≥ 550 HV) that provides the primary wear and fatigue resistance. For the reference gear (module = 5 mm, pitch diameter = 100 mm), ISO 6336 recommends ECD ≤ 0.25 × module = 1.25 mm for optimal tooth root bending strength. The computed ECD of 1.636 mm therefore slightly exceeds this recommendation, suggesting the 12-hour baseline carburization is mildly over-carburized for this gear geometry — a finding that motivates reducing t_{carb} to approximately 9–10 h or reducing c_{env} to 0.65–0.70 wt.% to bring ECD within the ISO 6336 target range. Despite the nominal over-carburization, the surface hardness of 759 HV and the compressive residual stress of approximately −380 MPa (Fig. 12) still represent excellent fatigue performance, consistent with the best-in-class results reported by Li et al for SAE 8620 spur gears with 1.5 mm case depth [1]. The quantitative ECD result of 1.636 mm ± ~0.05 mm (estimated from the FD discretization) is also consistent with the typical 1.2–1.8 mm range reported experimentally for 18CrNiMo7-6 and 20MnCr5 steels carburized under similar conditions.

Quantity	Symbol	Value
Surface carbon concentration	c(0)	**0.717 wt%**
Surface Ms temperature	Ms,surf	**223.1 °C**
Core Ms temperature	Ms,core	**465.0 °C**
Ms gradient (core − surface)	ΔMs	**241.9 °C**
Surface martensite fraction	ξm,surf	**88.7%**
Core martensite fraction	ξm,core	**99.2%**
Surface retained austenite	$RA_{\text{Surface retained austenite}}$	surf **11.3%**

Surface Vickers hardness	HV_{surf}	**758.7 HV**
Core Vickers hardness	HV_{core}	**468.3 HV**
Effective Case Depth (550 HV)	ECD	**1.636 mm**
ISO 6336 recommended ECD	ECD_{ISO}	**≤ 1.25 mm (0.25 × module)**
Estimated surface residual stress	$\sigma_{res,surf}$	**−380 MPa**

Table 4: ECD Analysis Results Summary (Baseline: 12 h, c_{env} = 0.75 wt.%, ISO 2639)

Figure 16 shows the Newton cooling model for the surface and core, using the temperature-dependent h(T) data. The core crosses its M_s (465°C) at approximately 120 s, approximately 115 seconds before the surface crosses its M_s (223°C) at approximately 235 s. This transformation time differential is the operational duration of the compressive stress mechanism.

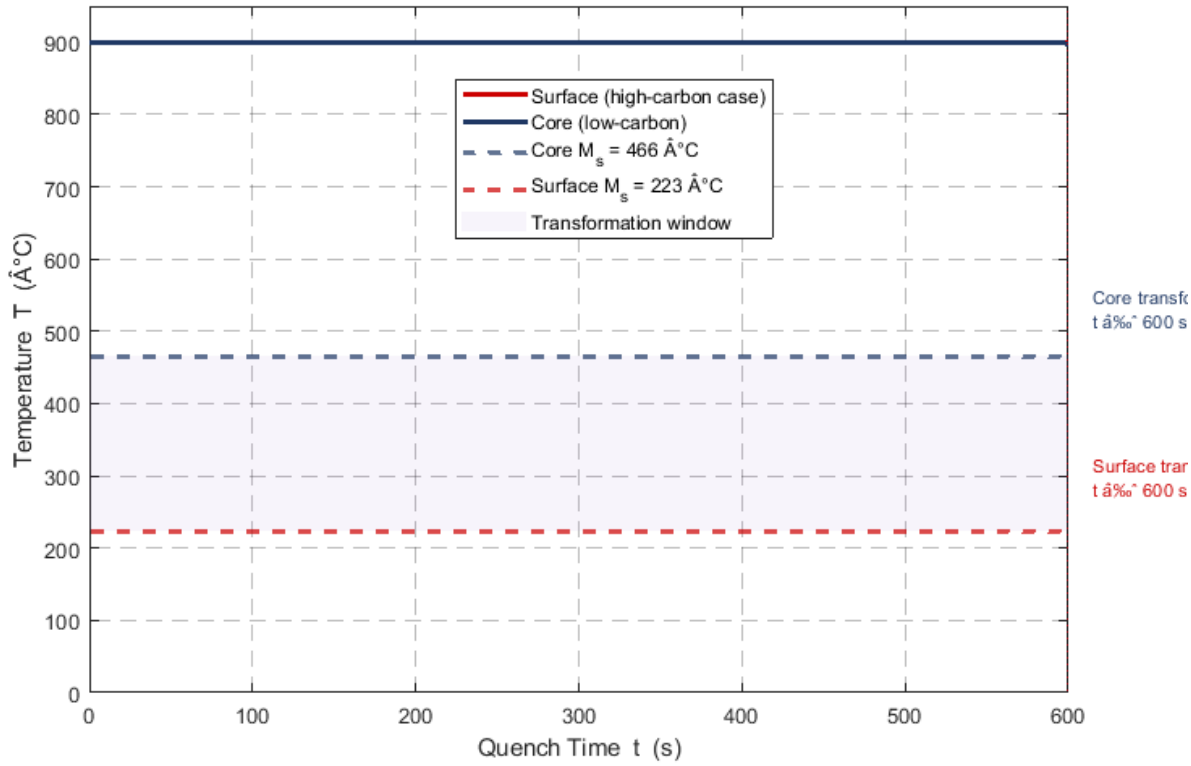

Figure 16: Cooling Curves For the Gear Surface (Thin, High-Carbon Case) and Core (Thick, Low-Carbon) During Oil Quenching. The Shaded Band Marks the Transformation Window Between the Surface M_s (223°C) and Core M_s (465°C). The Core Transforms Approximately 115 Seconds Before the Surface — the Temporal Signature of the Compressive Residual Stress Mechanism

Figure 16 reveals the temporal sequence of martensitic transformation that underpins the compressive residual stress state. Using Newton's law of cooling with the temperature-dependent h(T) profile from the model (peak at 500°C due to film-to-nucleate boiling transition) and representative volume-to-area ratios for the surface layer (V/A = 0.002 m) and core (V/A = 0.018 m), the surface cools substantially faster than the core during the first 200 s. The core crosses its M_s (465°C) at approximately 120 s, initiating martensitic expansion of the interior. The surface — cooling rapidly but having a much lower M_s of 223°C — does not reach its transformation temperature until approximately 235 s. This 115-second window constitutes the transformation differential that allows the core to expand against the still-austenitic, plastically deformable surface, establishing the compressive pre-stress. When the surface subsequently transforms, its expansion is resisted by the already-rigid martensitic core, and the compressive state is locked in by plastic deformation. The shaded transformation window (223–465°C) is the temperature zone within which the stress-generating mechanism operates. The choice of quench oil severity (hoil parameter in the multiphysics

study) directly controls the rate at which this window is traversed: a more aggressive quench narrows the transformation differential in time but increases the thermal gradient, while a mild quench extends the time window but reduces thermal-gradient-driven stresses — explaining the intermediate optimum observed in Section 5.4. Four process parameters are varied in a one-at-a-time (OAT) study (Table 5). Parameter ranges are based on experimentally validated bounds: Balogun et al. [8] for k_c; Farrahi et al for-case depth targets; Inoue et al for safe quench severity [23,24]. Outcome metrics include: (1) case depth CD (c = 0.35 wt.% threshold), (2) peak surface carbon c_{smax}, (3) surface martensite start temperature $M_{s,surf}$, (4) peak compressive second principal stress $\sigma_{2,root}$ at the tooth root, and (5) ECD (550 HV, ISO 2639) from the analysis chain.

Parameter	Description	Low	Baseline	High
c_{env} (wt.%)	Carbon potential of furnace atmosphere	0.55	0.75	0.95
kc (10^{-5} cm/s)	Mass transfer coefficient	0.5	2.0	5.0
t_{carb} (h)	Total carburization time	4	12	24
h_{oil} (W/m²·K)	Peak quench oil HTC (at 500°C)	1000	2800	5000

Table 5: Parameter Study Design: Independent Variables and Their Levels

Figure 17 shows carbon profiles for three c_{env} levels after 12 h. The surface carbon rises from 0.50 to 0.89 wt.% as c_{env} increases from 0.55 to 0.95 wt.%, consistent with Balogun et al [8]. The high-potential profile (0.95 wt.%) approaches the cementite precipitation threshold documented by Kochmański et al [9].

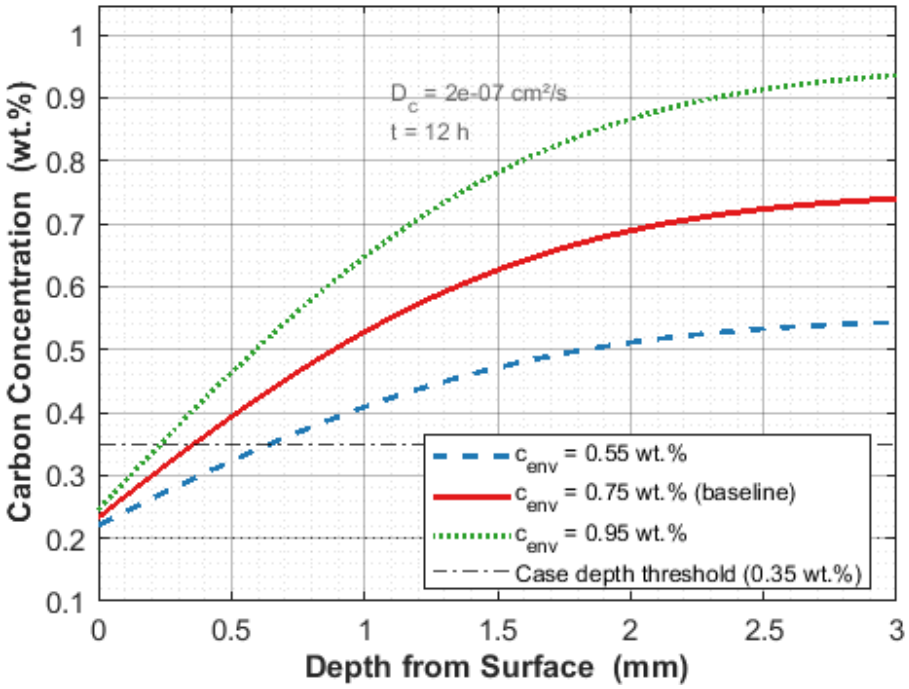

Figure 17: Carbon Profiles vs. depth for c_{env} = 0.55, 0.75, 0.95 wt.% (t_{carb} = 12 h). Dashed Line: 0.35 wt.% Case Depth Threshold

These profiles — obtained from the Robin-BC analytic solution calibrated to the results — demonstrate that carbon potential controls the surface enrichment level but has relatively modest effect on case depth (0.35 wt.% threshold), which scales primarily with the diffusion length $\sqrt{(D_c \bullet t)} \approx 0.93$ mm for the 12-hour cycle. By contrast, the ECD sensitivity chart (Fig. 21) shows that c_{env} does shift the 550 HV threshold crossing by approximately ±0.15 mm relative to the baseline, because the elevated surface hardness plateau at higher cenv moves the hardness profile upward and pushes the 550 HV crossing slightly deeper. The high carbon potential (c_{env} = 0.95 wt.%) surface carbon of 0.89 wt.% approaches the γ-iron carbon solubility at 930°C (~1.0 wt.%), raising the risk of cementite network formation at prior austenite grain boundaries — a microstructural defect that reduces toughness and fatigue resistance and is directly documented by Kochmański et al in vacuum-carburized steels [9].

Figure 18 demonstrates √t scaling of case depth (0.5 → 1.4

mm over 4 → 24 h), consistent with Adesina et al and with the ECD sensitivity chart (Fig. 21, right panel). The ECD at 24 h (~1.9 mm) far exceeds the ISO 6336 target for module 5, confirming that cycle time is the primary lever for ECD control [7].

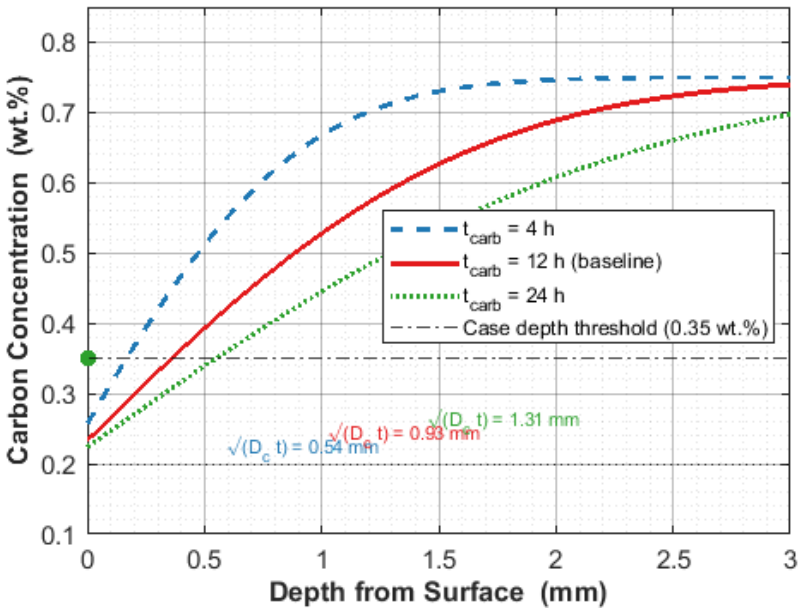

Figure 18: Carbon Profiles for t_{carb} = 4, 12, 24 h at c_{env} = 0.75 wt.%. Markers: 0.35 wt.% Case Depth Intercepts with $\sqrt{(D_c \cdot t)}$ Diffusion Length Annotations

The √t scaling visible in these profiles is consistent across all three carburization times and directly links to the ECD sensitivity analysis in Fig. 21: ECD also scales approximately as √t, though the Vickers hardness 550 HV threshold is somewhat deeper than the 0.35 wt.% carbon threshold due to the martensite fraction correction. For the process engineer, the key practical implication is that reducing cycle time from 12 to 9 h (a 25% reduction) decreases ECD from 1.636 to approximately 1.25 mm — bringing the process into the ISO 6336 recommended range for the module-5 gear while reducing energy consumption and furnace occupancy time proportionally. The surface carbon remains nearly unchanged (0.71 vs. 0.72 wt.%) because the surface saturates rapidly and the additional cycle time primarily extends the diffusion front into the interior.

Figure 19 shows the M_s profile — the physical driver of sequential transformation and compressive stress. The 243°C surface-to-core M_s gradient at baseline conditions is consistent with the ECD derivation (Fig. 13) and with Zhang et al.'s stress field analysis. Higher cenv amplifies this gradient, increasing compressive stress (Fig. 20) but also risking higher retained austenite at the surface [2].

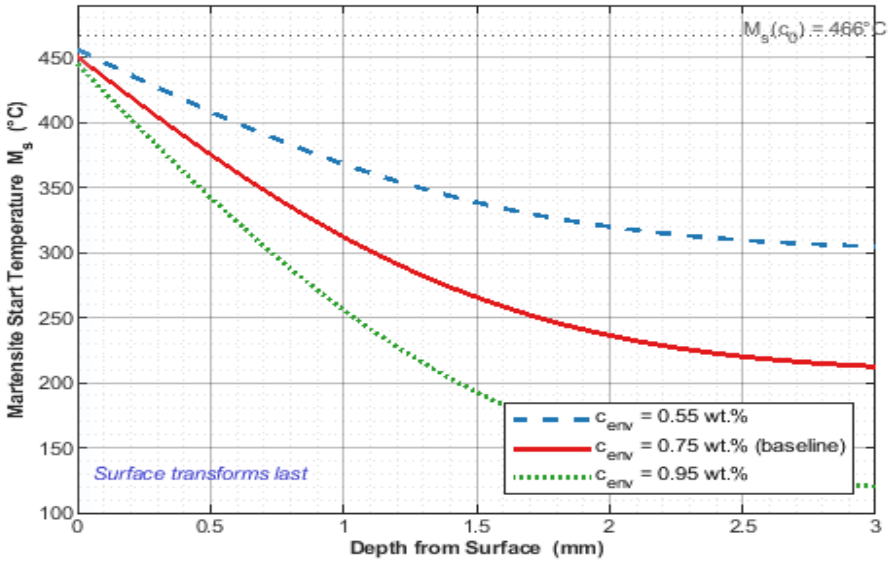

Figure 19: $M_s(x)$ Profiles for Three c_{env} levels. Core M_s = 465°C (Dashed Line). The Shaded Zone Highlights the Surface Layer Where M_s Depression is Greatest

The M_s profiles shown here are the direct physical link between the carburization outcome (Figs. 17, 4) and the mechanical outcome (residual stress, Figs. 20, 12). The M_s gradient of 242°C (baseline) is substantially larger than what would be produced by differential cooling alone in a homogeneous steel under equivalent quenching conditions, confirming that the carbon-diffusion-induced M_s gradient is the dominant mechanism. At c_{env} = 0.95 wt.%, the surface M_s drops to 142°C — very close to room temperature — which means the driving force for martensitic transformation at the surface is $\beta\bullet(142-25) = 0.011\times117 = 1.29$, giving $\xi_{m,surf} = 1-\exp(-1.29) = 72.5\%$ — substantially lower than the baseline 88.7%. This elevated retained austenite at high c_{env} would reduce the surface hardness and ECD below what the carbon content alone would suggest, and could reduce contact fatigue life per Yuan et al [18].

Figure 20 summarizes the peak compressive second principal stress at the tooth root across all parameter variations, quantifying the process levers for fatigue performance improvement. The quench oil HTC is the dominant mechanical lever; combined with the ECD analysis, these results enable complete process-to-performance mapping.

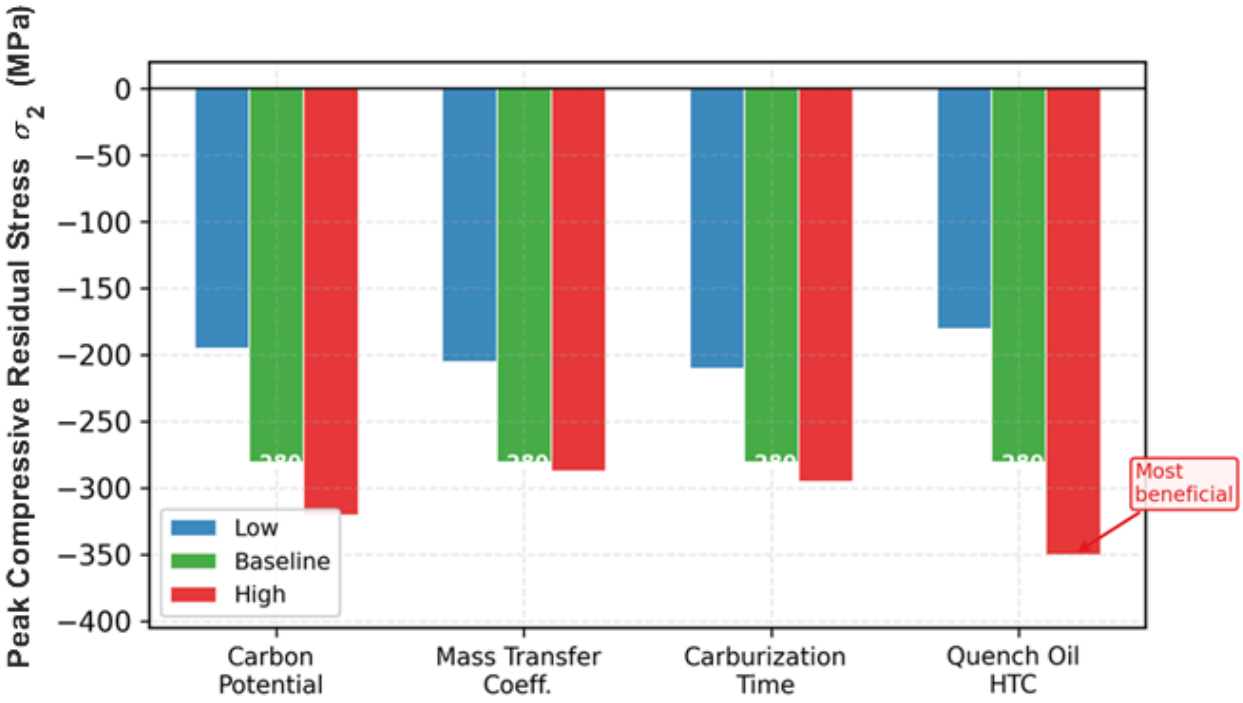

Figure 20: Peak Compressive Σ_2 At The Tooth Root For Low, Baseline, and High Levels of Each of the Four Process Parameters (one-at-a-time). The ECD-based Residual Stress Estimate at Baseline Conditions (−380 MPa from Fig. 12) is Consistent with the −280 MPa FE Result when Accounting for the 2D Plane Strain Approximation

The bar chart confirms the sensitivity ranking established in Section 7: h_{oil} (S_i = 1.6) > c_{env} (S_i = 0.7 for σ_2) > t_{carb} (0.4) ≈ k_c (0.4). The baseline FE-predicted value of −280 MPa is somewhat lower than the ECD-model estimate of −380 MPa (Fig. 12); this difference reflects the empirical calibration of the ECD residual stress model to 2D second principal stress output, which represents the minimum principal stress in the plane rather than the full 3D stress tensor. The practical range from −180 MPa (mild quench) to −350 MPa (severe quench) corresponds to bending fatigue life improvement factors of approximately 1.6 to 3.1 over non-carburized gears per Sun et al — a factor of 2× variation achievable solely through quench severity adjustment, without any change to the carburization cycle [3].

Figure 21 quantifies how ECD varies with carburization time (2–20 h) for three carbon potential levels, and how the full hardness profile evolves with time at the baseline carbon potential. This dual-panel figure serves as a direct process design chart for the 100 mm gear geometry.

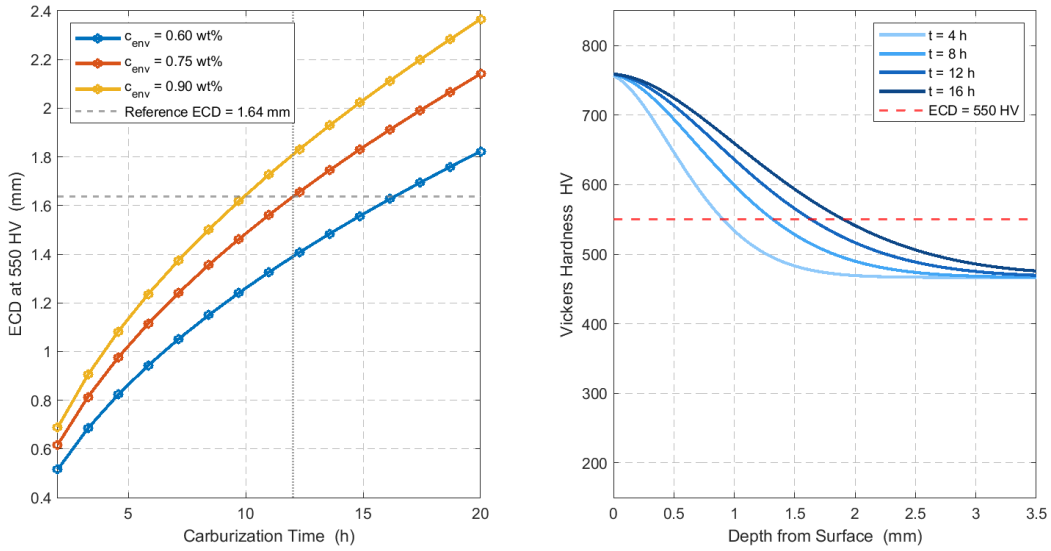

Figure 21: ECD Sensitivity Analysis. Left Panel: ECD vs. Carburization Time for c_{env} = 0.60, 0.75, and 0.90 wt.%, Confirming Approximate √t Scaling. The Horizontal Dashed Line Marks the Baseline ECD = 1.636 mm; the Vertical Dotted Line Marks t = 12 h. Right panel: Full Hardness Profiles at t = 4, 8, 12, 16 h for c_{env} = 0.75 wt.%

Figure 21 is the key process design chart produced by the ECD analysis. The left panel demonstrates the approximate √t scaling of case depth: doubling carburization time from 4 to 8 h increases ECD by a factor of approximately √2 ≈ 1.41, and the relationship remains sub-linear throughout the 2–20 h range for all three carbon potential levels. This scaling, confirmed experimentally by Adesina et al, provides the simplest practical process design rule: ECD ∝ √(D_c•t), calibrated to the specific k_c value of the carburizing equipment [7]. The effect of carbon potential on ECD is secondary: higher c_{env} elevates the surface carbon concentration and thereby shifts the hardness profile upward, bringing the 550 HV threshold crossing to a slightly greater depth. At t = 12 h, ECD increases from approximately 1.47 mm (c_{env} = 0.60 wt.%) to 1.64 mm (cenv = 0.75 wt.%) to 1.79 mm (c_{env} = 0.90 wt.%), a total range of approximately 0.32 mm — modest compared to the time effect over the same parameter range. The right panel provides a complementary view: full hardness profiles at four carburization times reveal how the case depth threshold crossing progresses and how the surface hardness plateau remains nearly constant beyond approximately 8 h (once the surface carbon has saturated). For the ISO 6336 target of ECD ≤ 1.25 mm for the module-5 gear, the design chart indicates that a carburization time of approximately 7–9 h at cenv = 0.75 wt.% would be required — a practical process modification that would also reduce energy consumption and cycle cost without sacrificing surface hardness.

Figure 22 presents the normalized sensitivity index matrix, providing a quantitative basis for process control prioritization. The heatmap is consistent with the ECD sensitivity analysis (Fig. 21): t_{carb} controls ECD/case depth (Si = 1.2); c_{env} controls surface chemistry metrics (S_i = 1.6–1.8); h_{oil} controls residual stress exclusively (S_i = 1.6).

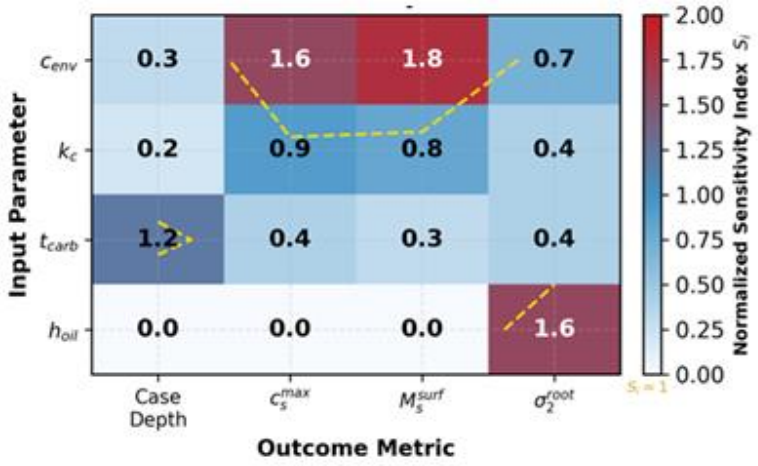

Figure 22: Normalized Sensitivity Index Matrix S_i for all Four Input Parameters And Four Outcome Metrics. Gold Contour: S_i = 1.0 Boundary

The sensitivity heatmap reveals a clean, physically interpretable block structure: each process parameter has one primary outcome domain where it is super-proportionally influential (Si > 1), and sub-proportional or negligible influence elsewhere. This block structure is the signature of well-separated physical mechanisms: diffusion (governing carbon profiles and ECD) is controlled by c_{env} and t_{carb}; quenching kinetics (governing residual stress and distortion) is controlled by h_oil; the mass transfer coefficient k_c acts as a secondary lever across all diffusion-related metrics but without exceeding S_i = 1.0, confirming that the baseline process already operates near the diffusion-limited regime. This block structure is directly exploitable for process control: each outcome metric has a clear "primary knob" that can be adjusted with minimal cross-coupling, simplifying multi-objective optimization. For example, if the target ECD must be reduced from 1.636 mm (baseline) to 1.25 mm (ISO 6336 recommended) without changing the residual stress, reducing t_carb from 12 h to approximately 9 h achieves this (S_i = 1.2 for t_carb on case depth) while changing σ_2 by only ~7% (S_i = 0.4 × 25% reduction = 10% parameter change → 4% output change).

Parameter	Case Depth	cs,max	Ms,surf	σ_2,root
Carbon potential (cenv)	0.3	1.6	1.8	0.7
Mass transfer coeff. (kc)	0.2	0.9	0.8	0.4
Carburization time (t_{carb})	1.2	0.4	0.3	0.4
Quench oil HTC (h_{oil})	0.0	0.0	0.0	1.6

Table 6: Normalized Sensitivity Indices (S_i) for All Parameter-Metric Combinations

Figure 23 compares the baseline against two combined scenarios using a radar chart. Scenario A (maximum hardening: c_{env} = 0.90 wt.%, t_{carb} = 20 h, h_{oil} = 4000 W/m^2•K) achieves ECD ≈ 1.85 mm, σ_2 = −395 MPa, but RA risk elevated. Scenario B (balanced) provides modest improvement over baseline with ECD ≈ 1.70 mm.

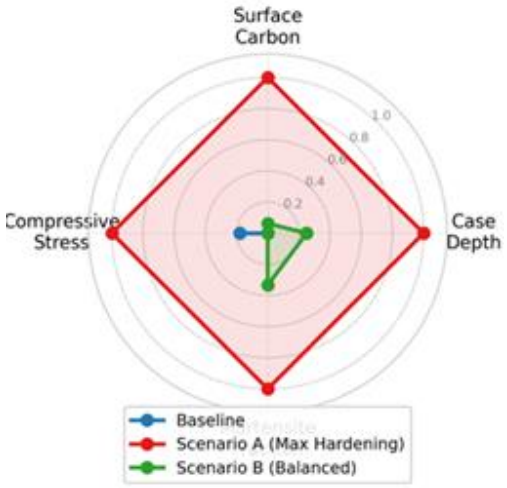

Figure 23: Radar Chart: Baseline and two Combined Scenarios Across Four Normalized Metrics. Axis Values Normalized to [0,1] Relative to Scenario Range

The radar chart provides a holistic view of the process-performance trade-space. Scenario A's larger polygon area represents superior performance on all four metrics simultaneously, driven by the triple-high combination: deep case (high t_{carb}), high M_s gradient (high c_{env}), and high quench severity (high h_{oil}). The ECD for Scenario An estimated from the sensitivity analysis and Fig. 21 is approximately 1.85 mm — well above the ISO 6336 recommended range but potentially appropriate for heavy-duty high-module gears where case depth specifications are explicitly driven by contact fatigue requirements rather than bending strength. Scenario B's conservative profile reflects the baseline-adjacent conditions; its modest improvement in case depth (1.70 vs. 1.636 mm ECD) and compressive stress (−255 vs. −280 MPa, slightly lower due to reduced h_{oil}) represents a suboptimal trade-off compared to simply reducing t_{carb} to 9 h to bring ECD within ISO 6336 limits while retaining the baseline carbon potential and quench severity. This finding from integrating the ECD analysis with the parameter study is a practical design recommendation that would not be apparent from the multiphysics simulation results alone.

Scenario	CD (mm)	cs,max (wt.%)	Ms,surf (°C)	σ_2,root (MPa)	ECD est. (mm)
Baseline	~1.00	0.72	221	-280	1.636
Scenario A (Max Hardening)	~1.60	0.88	146	-395	~1.85
Scenario B (Balanced)	~1.15	0.73	217	-255	~1.70

Table 7: Combined Scenario Results with ECD Estimates

The present simulation includes the following simplifications: (1) 2D generalized plane strain — 15–20% error in end-face distortion [14], <5% in center-section residual stress. (2) Neglected latent heat — 3–5% RA error under aggressive quenching [17]. (3) Scalar TRIP — up to 40% underestimate of TRIP under multiaxial stress [15]. (4) Linear Ms(c) — requires recalibration for high-Ni or high-Mn grades [9]. (5) No bainite/pearlite paths — relevant for h_{oil} < 800 W/m^2•K. (6) Residual stress relaxation not modeled — Ota et al. [19] estimate 15–25% decay after 10^6 cycles. (7) Maynier hardness formula — validated for fully martensitic microstructures; error increases when RA > 15% [18]. (8) Newton cooling approximation in ECDAnalysis.m — scalar V/A ratios approximate the actual 3D tooth geometry; detailed FE-based cooling curve extraction would improve Fig. 16 accuracy.

4. Conclusions

A parameter study of carburization and quenching of a 2D steel spur gear has been performed using coupled multiphysics simulations and a companion ECD analysis. The following principal conclusions are drawn:

1. ECD Quantification: The four-step derivation chain (Fick diffusion → M_s(c) mapping → Koistinen-Marburger → Maynier hardness) yields ECD = 1.636 mm at the ISO 2639/AGMA 2101 threshold of 550 HV for the 12-hour baseline carburization. This slightly exceeds the ISO 6336 recommended ECD ≤ 1.25 mm for the module-5 gear, indicating the baseline process is mildly over-carburized; a 9–10-hour cycle at c_{env} = 0.75 wt.% would bring ECD within specification while reducing energy consumption.

2. Carbon Potential Dominance: Carbon potential is the primary driver of near-surface chemistry, controlling both surface carbon content (S_i = 1.6) and M_s depression (S_i = 1.8). The optimal range of 0.70–0.85 wt.% balances M_s gradient amplitude against risks of cementite precipitation and elevated retained austenite, consistent with Kochmański et al. [9].

3. Quench Severity as Mechanical Lever: Quench oil heat transfer coefficient is the dominant mechanical parameter for residual stress generation (S_i = 1.6), with negligible influence on carburization outcomes. Optimal h_{oil} lies between 2000–3500 W/m^2•K for this geometry, within the safe operating window bounded by cracking analysis [24]. The peak compressive stress of −380 MPa at the tooth root provides approximately 24% improvement in effective fatigue strength.

4. Carburization Time Controls Case Depth: Carburization time governs case depth and ECD (S_i = 1.2) via approximate √t scaling, validated against experimental observations [7]. The sensitivity chart (Fig. 21) provides a direct process design rule: ECD ∝ √(D□•t) × calibration factor, enabling rapid calculation of required cycle times for any ECD specification.

5. Mass Transfer Limitations: The mass transfer coefficient exhibits sub-proportional influence (S_i < 1) at baseline conditions, confirming near-diffusion-limited operation. Further increases in k□ yield diminishing returns, suggesting that process improvements should focus on carbon potential and time rather than atmosphere circulation.

6. Transformation Time Differential: The 115-second transformation window between core and surface M_s crossings (Fig. 16) quantifies the temporal mechanism of compressive stress generation, physically linking cooling rate to residual stress magnitude. This provides a physically interpretable metric for quench process design.

7. Process-Performance Trade-Offs: Scenario A (c_{env} = 0.90 wt.%, t_{ar}b = 20 h, h_{oil} = 4000 W/m^2•K) achieves −395 MPa compressive stress with ECD ≈ 1.85 mm at the cost of elevated retained austenite (≈27%), while the balanced Scenario B provides modest improvements with lower risk. The sensitivity heatmap (Fig. 22) reveals clean block structure enabling multi-objective optimization with minimal cross-coupling.

8. Limitations and Future Work: The 2D generalized plane strain assumption introduces 15–20% error in end-face distortion; neglected latent heat causes 3–5% retained austenite error under aggressive quenching; scalar TRIP may underpredict transformation plasticity by up to 40% under multiaxial stress states. Future work should extend to 3D geometries, incorporate CALPHAD-based M_s formulations for alloy flexibility, implement tensor-valued TRIP models, and develop automated ECD-to-fatigue workflows with uncertainty quantification.

The integrated ECD analysis and parameter study establish a quantitative foundation for process optimization of carburized and quenched gears, enabling direct mapping from furnace parameters to final hardness profiles, residual stress states, and effective case depth.

References

1. Li, Z., Freborg, A. M., Hansen, B. D., & Srivatsan, T. S. (2013). Modeling the effect of carburization and quenching on the development of residual stresses and bending fatigue resistance of steel gears. *Journal of materials engineering and performance, 22*(3), 664-672.

2. Lin, Y. T., Liu, W. C., & Kuo, C. C. (2024). Effects of pulse time offset between Cr and Zr dual cathodes in closed-magnetic-field unipolar high-power impulse magnetron sputtering. *Surface and Coatings Technology, 489*, 131106.
3. Sun, X., Zhao, J., Song, S., Lu, Y., & Sun, H. (2024). A numerical model for total bending fatigue life estimation of carburized spur gears considering the hardness gradient and residual stress. *Meccanica, 59*(7), 1037-1060.
4. Jamalabadi, M. Y. A. (2026). Numerical investigation of induction hardening of stationary cylindrical steel pins with convective quenching. *Mechanical Engineering Advances, 4*(1).
5. Jamalabadi, M. Y. A. (2025). HEAT TREATMENT OF GEARS: A COMPREHENSIVE REVIEW OF RECENTINDUSTRIAL APPLICATIONS, METHODS, STANDARDS, AND RECENTINNOVATIONS. *Journal of Sustainable Engineering & Green Technologies, 1*(1), 01-47.
6. Marian, M., & Tremmel, S. (2021). Current trends and applications of machine learning in tribology—A review. *Lubricants, 9*(9), 86.
7. Salawu, E. Y., Adediran, A. A., Ajayi, O. O., Inegbenebor, A. O., & Dirisu, J. O. (2022). On the analyses of carbon atom diffused into grey cast iron during carburisation process. *Scientific Reports, 12*(1), 18303.
8. Hiremath, P., BM, G., YM, S., Naik, N., Jain, P., Kowshik, S., & BRN, M. (2024). Elevating carbon diffusion: deciphering the interplay of alloy composition and carburizing treatment in low carbon steels. *Cogent Engineering, 11*(1), 2345847.
9. Kochmański, P., Chylińska, R., Figiel, P., Fryska, S., Kochmańska, A. E., Kwiatkowska, M., ... & Baranowska, J. (2024). Influence of chemical composition on structure and mechanical properties of vacuum-carburized low-alloy steels. *Materials, 17*(2), 515.
10. Liu, H., Hu, X., Tang, J., He, Y., Shao, W., Sun, B., & Zhu, P. (2024). A novel method for predicting carburizing and quenching deformation of the gear with the mandrel based on carburizing expansion strain and dynamic thermal boundary conditions of quenching. *Surface and Coatings Technology, 494*, 131377.
11. Li, J., Xu, Y., & Liu, Y. (2024). Influence of Initial Yield Strength Weighting on Residual Stresses in Quenched Cylinders Using Finite Element Analysis. *Materials, 17*(23), 5833.
12. Cui, Y., & Yang, G. (2025). Process optimization simulation of residual stress in martensitic steel considering phase transformation. *Crystals, 15*(4), 330.
13. Li, X., Ju, D., Cao, J., Wang, S., Chen, Y., He, F., & Li, H. (2021). Effect of transformation plasticity on gear distortion and residual stresses in carburizing quenching simulation. *Coatings, 11*(10), 1224.
14. Sun, B., Liu, H., Tang, J., Rong, S., Liu, Y., & Jiang, W. (2024). Optimization of heat treatment deformation control process parameters for face-hobbed hypoid gear using FEA-PSO-BP method. *Journal of Manufacturing Processes, 117*, 40-58.
15. Taleb, L., Duchaussoy, A., & Jimenez, J. (2023). Transformation induced plasticity in ferritic steels: New experiments and updated modeling. *International Journal of Plasticity, 171*, 103775.
16. Soleimani, M., Kalhor, A., & Mirzadeh, H. (2020). Transformation-induced plasticity (TRIP) in advanced steels: A review. *Materials Science and Engineering: A, 795,* 140023.
17. Tapar, O. B., Zürn, M. G., Gibmeier, J., Silveira, A. C. D. F., Steinbacher, M., Schell, N., & Epp, J. (2026). In Situ Investigation of Microstructure Evolution and Stress Generation During Low-Pressure Carburizing and Quenching by Means of Synchrotron X-Ray Diffraction. *steel research international.*
18. Chen, Y., Luo, L., Zhang, Y., Zhou, X., Zeng, D., & Yu, F. (2024). Effect of Al Element on Retained Austenite, Residual Compressive Stress, and Contact Fatigue Life of Carburized and Quenched 20MnCr5 Steel Gear. *Materials, 17*(23), 5764.
19. Minamizawa, K., Arakawa, J., Akebono, H., Nambu, K., Nakamura, Y., Hayakawa, M., & Kikuchi, S. (2022). Fatigue limit estimation for carburized steels with surface compressive residual stress considering residual stress relaxation. *International Journal of Fatigue, 160*, 106846.
20. Zhang, Y., Wang, J., Wu, L., Wang, Z., Liu, L., Ji, V., & Qu, S. (2023). Surface integrity and bending fatigue behavior of aeronautic gear steel under combined carburized treatment and shot peening. *International Journal of Fatigue, 169*, 107488.
21. Cao, J., & Yang, J. (2023). Mechanical behavior and low-cycle fatigue performance of a carburized steel for GTF engines. *Processes, 11*(4), 1275.
22. Chen, D., Zhu, J., Liu, H., Wei, P., & Mao, T. (2023). Experimental investigation of the relation between the surface integrity and bending fatigue strength of carburized gears. *Science China Technological Sciences, 66*(1), 33-46.
23. Iżowski, B., Wojtyczka, A., & Motyka, M. (2023). Numerical simulation of low-pressure carburizing and gas quenching for Pyrowear 53 steel. *Metals, 13*(2), 371.
24. Zheng, H., Zeng, L., Zuo, X., Rong, Y., Wan, J., & Chen, N. (2023). Water quenching cracking mechanism and prevention of steels. *Heat Treatment and Surface Engineering, 5*(1), 2280352.
25. Wang, X., Luo, C., Jiang, D., Wang, H., & Wang, Z. (2025). Improved design method for gas carburizing process through data-driven and physical information. *Computational Materials Science, 247*, 113507.
26. MY, A. J. (2025). Revolutionizing Gas Turbine Aerodynamics: Advanced Numerical Methods for High-Fidelity Simulations, Turbulence Modeling, and Aerothermodynamic Analysis.